Stall-induced aeroelastic instability of floating offshore wind turbines
Comparison of frequency domain and time domain quasi-steady approaches

Meng, Qingshen; Yu, Wei; Wu, Faming; Hua, Xugang; Chen, Chao

DOI
10.1016/j.renene.2025.123174

Publication date
2025

Document Version
Final published version

Published in
Renewable Energy

Renewable Energy 251 (2025) 123174

Contents lists available at ScienceDirect

Renewable Energy

journal homepage: www.elsevier.com/locate/renene

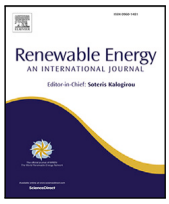

Stall-induced aeroelastic instability of floating offshore wind turbines: Comparison of frequency domain and time domain quasi-steady approaches

Qingshen Meng [a,b], Wei Yu [b], Faming Wu [c], Xugang Hua [a,*], Chao Chen [a,*]

[a] State Key Laboratory of Bridge Engineering Safety and Resilience, College of Civil Engineering, Hunan University, Changsha, 410006, China
[b] Flow Physics and Technology, Faculty of Aerospace Engineering, Delft University of Technology, Delft, 2629 HS, Netherlands
[c] Wind Power Business Division, CRRC Zhuzhou Institute Co.Ltd, Zhuzhou, 412000, China

ARTICLE INFO

Keywords:
Floating offshore wind turbines
Stall-induced instability
LCO
Control

ABSTRACT

With the increasing size of floating offshore wind turbines (FOWTs), stall-induced aeroelastic instability has become a critical issue. This study numerically investigates this instability for FOWTs at stand-still conditions using time and frequency domain approaches. A nonlinear aeroelastic model based on quasi-steady theory and a linearized version are used for time and frequency domain simulations, respectively. Hydrodynamic damping considers both radiation and viscous drag effects. The aeroelastic instability of a stand-still NREL OC3-Hywind 5MW FOWT is analyzed for various inflow yaw misalignment angles. Frequency domain simulation shows rotor edgewise and tower side-side modes exhibit stall-induced instability due to aerodynamic negative damping at specific yaw misalignment and azimuth angles. The platform's yaw mode also shows small negative damping, despite large hydrodynamic damping, while other platform modes remain dynamically stable. Safety margins of FOWTs are analyzed for multi-mode stability, and an active control strategy is proposed to prevent stall-induced instability in all unstable modes. Limit cycle oscillations in the rotor's in-out plane are observed from time domain simulation. Instability regions predicted by both analyses highly overlap, but frequency domain results are more conservative. Blade instability may cause high-frequency vibrations in platform movements with limited amplitudes and severe oscillations in tower structures.

1. Introduction

The escalation of energy crises and environmental concerns has stimulated a rise in the utilization of renewable energy sources, such as wind energy [1]. Remote offshore areas with high-quality wind resources have garnered significant interest from scientists and manufacturers. Developing floating wind farms is a cost-effective solution for harnessing wind energy in deep offshore regions [2]. However, the harsh conditions in the deep sea, characterized by extreme wind and wave patterns, render maintenance and repair of FOWTs very challenging [2,3].

The growing deployment of wind turbines offshore has also driven a significant increase in demand for larger wind turbines, with blade lengths now exceeding 137 m [4]. The increased size of wind turbine blades enhances their structural flexibility, leading to more significant challenges related to aeroelastic stability [5,6]. A recent field experiment has confirmed the risk of edge instability in a full-scale 7 MW wind turbine [7], underscoring the critical importance of addressing aeroelastic instability. Furthermore, Bortolotti et al. [8], emphasized that aeroelastic stability should be carefully considered during the design phase, proving aeroelastic stability design a critical factor in improving the life-long performance, which could become more significant compared to the currently dominant load-driven design [9]. Generally speaking, instability is a broad concept, which typically includes vortex-induced vibration (VIV) [10], blade pitch-flap flutter [11], stall-induced vibration [12], rotor-shaft whirl [13], and aeromechanical instability [14]. These instabilities may induce extreme structural responses, increase the stress on wind turbine components, contribute to fatigue damage, and ultimately reduce the turbine's lifetime. Among these instabilities, stall-induced vibration (also called stall-induced instability, generally caused by aerodynamic negative damping) is crucial for modern large-size wind turbines and has been studied systematically for stall-regulated wind turbines [12].

Historically, the framework for the analysis of instability induced by stalls in a quasi-steady perspective for onshore wind turbines has been constructed in the frequency domain before and after the first decade of the 21st century. This work is mainly attributed to Hansen [15,16] at DTU, etc. Hansen [15] and Chaviaropoulos [17] conducted their analyses based on linear structural dynamics, with the damping ratio

* Corresponding authors.
E-mail addresses: qsmeng@hnu.edu.cn (Q. Meng), W.Yu@tudelft.nl (W. Yu), cexghua@hnu.edu.cn (X. Hua), steinchen@hnu.edu.cn (C. Chen).

https://doi.org/10.1016/j.renene.2025.123174
Received 21 June 2024; Received in revised form 12 April 2025; Accepted 16 April 2025
Available online 9 May 2025

being the criterion for the instability of a specific mode. Damping ratios are typically determined by calculating state-space eigenvalues. Overall damping ratios, which include structural and aerodynamic damping for fixed-bottom wind turbines, are conventionally adopted as the assessment parameter for stall-induced instability.

The acquisition of linear damping matrices considering the influence of interaction between the inflow wind and structure is of utmost importance in wind turbine aeroelastic instability. Hansen [18] emphasized the importance of aerodynamic damping in predicting fixed-bottom wind turbine instability. Petersen et al. [12] derived the explicit aerodynamic damping matrices for a stall-regulated wind turbine, demonstrating that aerodynamic damping for an operating wind turbine is strongly related to each airfoil's lift and drag coefficients and the rotor rotating speed. Besides, Thomsen et al. [19] proposed an experimental method for edgewise-direction aerodynamic damping determination and implemented it on a Bonus wind turbine. Chen et al. [20] developed a wavelet-based linearization method to evaluate aerodynamic damping for an operating wind turbine. FAST is considered capable of obtaining aerodynamic damping in a numerical way [21,22], by using central difference equations, allowing us to determine damping matrices at any possible operating position.

Beyond the traditional scope of quasi-steady instability research, recent studies have extended to include unsteady aerodynamic phenomena [23]. Among these, dynamic stall has emerged as a critical area of interest due to its profound impact. Quasi-steady stall-induced instability analysis typically relies on 2D steady-state polars to estimate aerodynamic damping [24]. However, blade vibrations can trigger dynamic flow separation, creating hysteresis loops in the lift and drag coefficients. These dynamic loads significantly influence the aerodynamic damping of the structure [25]. Extensive research has been devoted to understanding dynamic stall and its role in aerodynamic damping. For instance, Meng et al. [26] introduced a reduced-order floating wind turbine model incorporating the Beddoes-Leishman dynamic stall model and conducted stability analysis on the IEA 15 MW turbine with a spar-buoy platform. Similarly, Branlard et al. [23] enhanced the OpenFAST linearization module by integrating dynamic inflow and dynamic stall effects. Lohmann [27] investigated the differences among several dynamic stall models in predicting the amplitudes of stall-induced instability limit cycle oscillations (LCO), this study revealed that the amplitude-dependent aerodynamic positive damping, resulting from the dynamic stall effect, can constrain the growth of instability caused by steady stall. These studies prove that aerodynamic unsteadiness can affect the aerodynamic damping of an operating wind turbine.

Besides aerodynamic damping, previous studies also aimed at linearizing hydrodynamic forces for floating platforms. For example, ECN [28] released a linearized version of Morison's equation that accounts for current velocity and structural displacements. Li et al. [29] derived an analytical approach to determine radiation damping for a cylinder that emerges in the water, although this method cannot account for the influences from the tapered sections. Meng et al. [30] presented a linear approach to determine the analytical expression of viscous hydrodynamic damping for a spar-type floating wind turbine under different wave states.

Regarding stability studies of full-size wind turbines, researchers have conducted detailed stability analyses for onshore wind turbines. For instance, Wang et al. [31] found that when yaw misalignment occurs, a DTU 10 MW stand-still wind turbine faces a higher possibility of stall-induced vibration as the local angle of attack (AoA) of a specific blade airfoil section exceeds 22°. Similar conclusions were drawn by Chen et al. [32]. Bir et al. [9] investigated wind turbine instability for both operating and stand-still situations, observing that a parked wind turbine is at higher risk of instability, especially under the DLC 7.1a of IEC standards (parking in extreme wind). Hansen [33] highlighted that stall-induced vibrations at stand-still for commercial pitch-regulated wind turbines remain a state-of-the-art topic. Volk et al. [7] conducted a field test to validate the edgewise instability of a 7 MW wind turbine, confirming that results from time domain simulations align well with field measurements.

Studies on stall-induced vibration and instability in pitch-regulated large floating offshore wind turbines were not published until 2007. Bir et al. [9] noted that stall-induced instability occurs in blade edgewise, tower side-side, and platform (barge floater) yaw modes, which can be highly destructive if ignored. Moreover, hydrodynamic effects in analyzing FOWT instability are gaining attention. Men et al. [6] proposed an identification method that allows for eigenvalue analysis of FOWT considering wave effects, implemented in the OpenFAST software. They discussed the instability properties of both offshore (OO-Star semi-submersible platform) and onshore wind turbines using this tool. Additionally, damping enhancement devices for FOWTs have been explored in recent years. For example, Aboutalebi et al. [34] introduced an oscillation water column design concept for a semisubmersible FOWT, showing significant damping improvement at several platform modes, proving its potential for platform dynamic stability control.

Despite significant advances, analytical tools with explicit expressions for FOWT stability research remain underexplored and underdeveloped, creating a notable demand in this field. To address this gap, the authors developed AeroHor, a simulation tool comprising nonlinear (AeroHor-nonlinear) and linear (AeroHor-linear) modules, which facilitates both time and frequency domain analyses. AeroHor is a simulation platform designed for structural (high-fidelity), aerodynamic, and hydrodynamic evaluations of onshore and offshore wind turbines, with an emphasis on computational efficiency. This tool integrates an advanced servo module that employs both nonlinear and state-space expressions, enabling users to conduct efficient wind turbine design and performance assessments. AeroHor is being developed to ensure compatibility with all IEC-defined design load cases and to enhance reliability under complex operational conditions. This study employed AeroHor to conduct both time and frequency domain analyses, identified instability regions for FOWTs, proposed an active control strategy for stall-induced instability mitigation, and reproduced the LCO phenomenon.

Given that a spar-type platform is one of the most promising solutions for floating wind turbine support structures, this paper focuses on the NREL OC3-Hywind 5 MW wind turbine, providing specific data on platform instability and revealing certain phenomena in FOWT instability using the developed tool. This paper is organized as follows: Section 2 presents the methodology for finite element (FE) model development and introduces the system equation of motion (EoM). It also outlines the theories for time domain simulations and systematically describes both the aerodynamic model based on quasi-steady theory and the approach for determining hydrodynamic loads. Section 3 linearizes aerodynamic loads into damping matrices and provides a method for calculating the damping ratio in state-space. Section 4 verifies the model to demonstrate the accuracy of both the linearized and nonlinear models. Section 5 presents the results of linear stability analysis for an OC3 5 MW floating wind turbine. Section 6 discusses the nonlinear time domain instability responses, reinforcing the conclusions drawn from the frequency domain analyses in Section 5. Finally, Section 7 concludes the paper.

2. Nonlinear model for time domain stability analysis

Stall-induced aeroelastic instability is typically analyzed using both frequency and time domain approaches. The frequency domain method offers a rapid and quantitative means of understanding the instability phenomenon from a global perspective, making it particularly convenient during the early stages of wind turbine design. Despite its higher computational cost and limited applicability in early design phases, the time domain method plays a crucial role in validating potential instability conditions identified by the frequency domain approach. Therefore, a combined approach is recommended: the frequency domain method can be used initially for a preliminary risk assessment

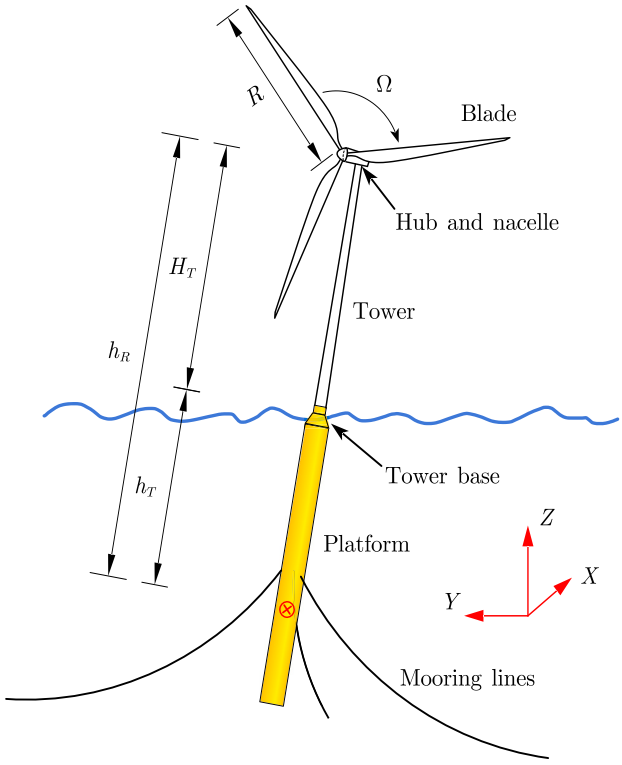

Fig. 1. Spar-type floating wind turbine structural layout.

of stall-induced instability during the design phase, followed by the time domain method for response verification under critical instability scenarios. Given that the frequency domain method represents a linearized approximation of the time domain method, this section begins by introducing the theory of the time domain nonlinear approach.

2.1. General description and coordinate system setup

While more advanced benchmark models with larger rotors, such as the IEA 15 MW wind turbine [35], have been released, this study employs the OC3 5 MW wind turbine developed by NREL [36,37] as the case-study wind turbine, primarily because of its extensive validation dataset available in the literature. A FE model is developed to simulate the dynamic behavior of the FOWT, described in this section.

A floating horizontal-axis wind turbine mainly contains a rotor, a hub, a nacelle, a tower, a platform, and a mooring system to constrain the floater's motion [37]. These components are shown in Fig. 1 with detailed parameters listed in Table 1. Six coordinate systems (CSs) are defined for the model as shown in Fig. 2, of which two of them are defined for describing platform (X, Y, Z and X', Y', Z') motions, and they are located in the platform center of gravity. One (x_t, y_t, z_t) is fixed at the tower base to describe tower fore-aft (FA) and side-side (SS) motions. Each blade has its own CS, which is mounted at blade roots and is named as $x_{b,j}, y_{b,j}, z_{b,j}$. Their directions can be seen in Fig. 2. However, to better locate the flexible bodies (blades and tower, modeled as Euler–Bernoulli beam), the X, Y, Z axes are rotated to X', Y', Z' by a transfer matrix **Rot**, its expression will be given in Appendix A.

2.2. Equation of motion

AeroHor adopts the Euler–Bernoulli beam to account for tower and blade flexibility. As the platform is considered a rigid body, and is

Table 1
Structural properties of the NREL-5 MW spar-type FOWT [35,36].

Rotor radius, R	63 m
Rated rotor speed, Ω	1.267 rad/s
Length from rotor centre to spar mass centre, h_R	168 m
Length from tower top to spar top, H_T	87.6 m
Length from tower base to spar mass centre, h_T	78 m
Lumped mass at tower top, M_0	3.5×10^5 kg
Platform diameter	9.4 m
Platform depth below SWL	120 m
Water depth	320 m
Length from spar bottom to spar mass centre, h_B	42 m
Platform mass, including Ballast	7466330 kg
Additional yaw spring stiffness	9.834×10^7 Nm/rad
Number of mooring lines	3
Depth to fairleads below SWL	70.0 m
Radius to anchors from platform centreline	853.87 m
Unstretched mooring line length	902.2 m

coupled with tower and blade elements, the overall EoM needs to be derived through the Euler–Lagrange equation:

$$\frac{\mathrm{d}}{\mathrm{d}t}\left(\frac{\partial \mathcal{T}}{\partial \dot{\mathbf{x}}}\right) - \frac{\partial \mathcal{T}}{\partial \mathbf{x}} + \frac{\partial \mathcal{V}}{\partial \mathbf{x}} = \mathbf{F} - \mathbf{C}_{\mathrm{s,r}}\dot{\mathbf{x}} \tag{1}$$

where $\mathcal{T}$ is the system kinetic energy, while $\mathcal{V}$ is the potential energy of the FOWT, and $\mathbf{x}$ represents the degree of freedom(DOF) vector, defined as:

$$\mathbf{x} = \{x_{b,i,j}, y_{b,i,j}, z_{b,i,j}, \theta_{b,x,i,j}, \theta_{b,y,i,j}, \theta_{b,z,i,j} \cdots x_{t,i}, y_{t,i}, z_{t,i}, \theta_{t,x,i}, \theta_{t,y,i}, \theta_{t,z,i} \cdots U_1, U_2, U_3, U_4, U_5, U_6\}^{\mathrm{T}} \tag{2}$$

in which i represents the i^{th} element and j is the j^{th} blade.

Besides, $\mathbf{F}$ is the general expression of the overall force vectors, and $\mathbf{C}_{\mathrm{s,r}}$ represents the Rayleigh damping matrix.

Appendix A determines the expression of $\mathcal{T}$ and $\mathcal{V}$. Insert $\mathcal{T}$ and $\mathcal{V}$ into Eq. (1) and the EoM of the FOWT model can be finally written as the following form: [38,39]

$$\mathbf{M}_{\mathrm{s}}\ddot{\mathbf{x}}(t) + \mathbf{C}_{\mathrm{s}}\dot{\mathbf{x}}(t) + \mathbf{K}_{\mathrm{s}}\mathbf{x}(t) = \mathbf{F}_{\mathrm{Aero}}(t) + \mathbf{F}_{\mathrm{Buoy}}(t) + \mathbf{F}_{\mathrm{Hydro}}(t) + \mathbf{F}_{\mathrm{Moor}}(t) + \mathbf{F}_{\mathrm{Gra}}(t) \tag{3}$$

where the $\mathbf{M}_{\mathrm{s}}$, $\mathbf{C}_{\mathrm{s}}$, and $\mathbf{K}_{\mathrm{s}}$ represent mass, damping, and stiffness matrices, respectively. Their expressions can be found in Appendix A. Additionally, the Rayleigh damping is proportional to the $\mathbf{M}_{\mathrm{s}}$ and $\mathbf{K}_{\mathrm{s}}$ following the relationship $\mathbf{C}_{\mathrm{s,r}} = \alpha_r \mathbf{M}_{\mathrm{s}} + \beta_r \mathbf{K}_{\mathrm{s}}$, and the coefficients α_r and β_r can be obtained according to Ref. [40]. Force vectors on the right side of the equation account for the loads acting on the complex FOWT system: loads from wind (Aero), still water (Buoy), waves (Hydro), mooring system (Moor), as well as gravity loads (Gra).

2.3. Aerodynamic force for a stand-still FOWT

For a stand-still wind turbine, airfoils are solely influenced by the incoming flow, unaffected by rotational effects. The vibration velocities of the FOWT components also influence the relative wind speed experienced by the blade elements. Similar to operational conditions, determining the loads on a wind turbine at a stand-still can be achieved through various methods, including high-fidelity aeroelastic coupled computational fluid dynamics (CFD), and low-fidelity aeroelastic drag-lift formula (BEM-like) model. This study opts for the quasi-steady BEM-like method for its computational efficiency. The airfoils' quasi-steady aerodynamic loads can then be determined by making use of the aerodynamic lift and drag coefficients definition equations [41]:

$$\begin{aligned} \mathrm{d}L(r,\alpha) &= \frac{1}{2}\rho_a c(r) V_{\mathrm{rel}}^2(r) C_l(r,\alpha)\mathrm{d}r \\ \mathrm{d}D(r,\alpha) &= \frac{1}{2}\rho_a c(r) V_{\mathrm{rel}}^2(r) C_d(r,\alpha)\mathrm{d}r \end{aligned} \tag{4}$$

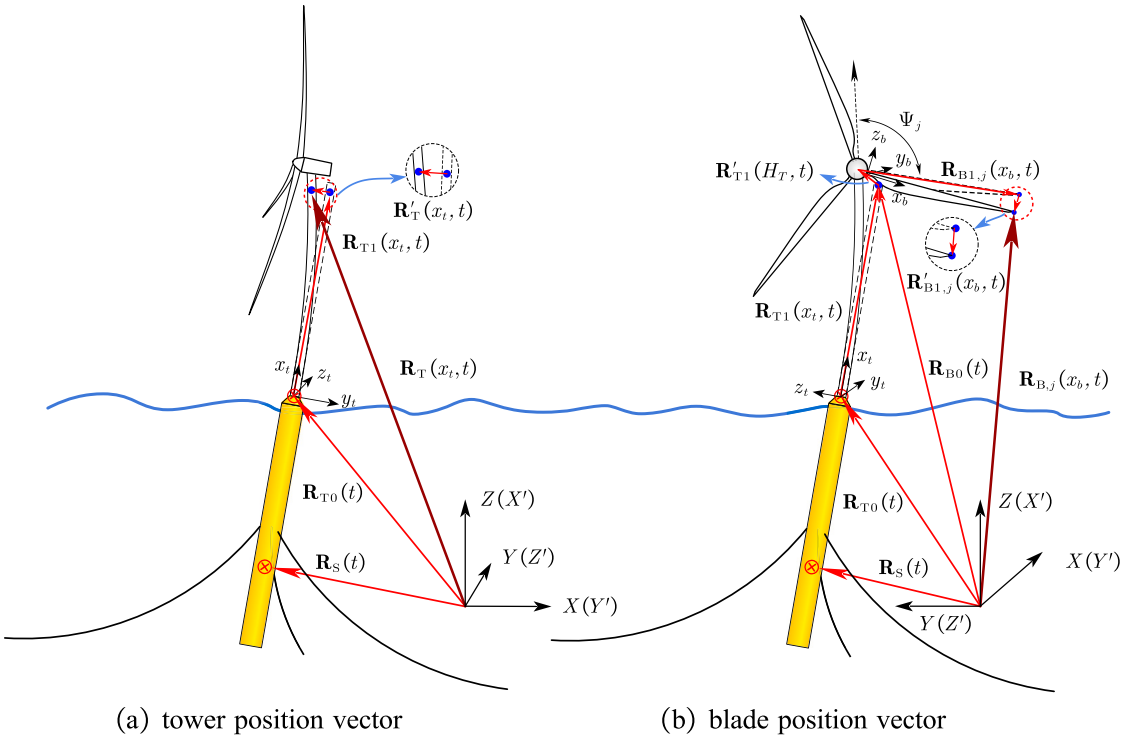

(a) tower position vector (b) blade position vector

Fig. 2. FOWT tower (a) and blade (b) flexibility and deformation.

in which the wind velocity V_{rel} is:

$$V_{\mathrm{rel}}^2 = V_{By,i,j}^2 + V_{Bz,i,j}^2 \tag{5}$$

where the $V_{By,i,j}$ and $V_{Bz,i,j}$ represent the perceived wind speed along y_b and z_b directions considering the coupling effect with FOWT vibrations respectively, their accurate expressions can be derived utilizing the following wind speed vectors equation:

$$\mathbf{V}_{\mathrm{B}}^{\mathrm{wind}} = \mathbf{V}_0 - \mathbf{T}_j\left(\widetilde{\mathbf{A}}_j\mathbf{Rot}^{\mathrm{T}}\dot{\mathbf{U}} + \widetilde{\mathbf{A}}_t\dot{\mathbf{u}}^{\mathrm{top,e}}\right) - \mathbf{T}_\beta\dot{\mathbf{v}}^{\mathrm{e}} \tag{6}$$

in which,

$$\begin{aligned}
\widetilde{\mathbf{A}}_t &= \mathbf{A}\left(\mathrm{d}x = x_b\cos\Psi_j,\ \mathrm{d}y = 0,\ \mathrm{d}z = -x_b\sin\Psi_j\right)\\
\dot{\mathbf{U}} &= \left\{\dot{\mathrm{U}}_1,\dot{\mathrm{U}}_2,\dot{\mathrm{U}}_3,\dot{\mathrm{U}}_4,\dot{\mathrm{U}}_5,\dot{\mathrm{U}}_6\right\}^{\mathrm{T}}\\
\dot{\mathbf{u}}^{\mathrm{top,e}} &= \left\{\dot{x}_t^{\mathrm{top}},\dot{y}_t^{\mathrm{top}},\dot{z}_t^{\mathrm{top}},\dot{\theta}_{t,x}^{\mathrm{top}},\dot{\theta}_{t,y}^{\mathrm{top}},\dot{\theta}_{t,z}^{\mathrm{top}}\right\}^{\mathrm{T}}\\
\dot{\mathbf{v}}^{\mathrm{e}} &= \left\{\dot{x}_{b,i,j},\dot{y}_{b,i,j},\dot{z}_{b,i,j},\dot{\theta}_{b,x,i,j},\dot{\theta}_{b,y,i,j},\dot{\theta}_{b,z,i,j}\right\}^{\mathrm{T}}
\end{aligned} \tag{7}$$

Eq. (6) accounts for the fact that the perceived wind speeds of blade elements are dominated by the inflow wind speed vector $\mathbf{V}_0$, FOWT movements: $\dot{\mathbf{U}}$, $\dot{\mathbf{u}}^{\mathrm{top,e}}$, and $\dot{\mathbf{v}}^{\mathrm{e}}$ representing the vibrating speed of the platform, tower top, and blade sections, in local CS, respectively. Furthermore, $\mathbf{T}_\beta$ is adopted to consider the influences of pitch angle β, $\mathbf{T}_j$ is the transformation matrix mainly due to azimuth angle. Expression for $\mathbf{A}$ can befound in Appendix A. Thus, $V_{By,i,j}$ and $V_{Bz,i,j}$ can be expanded as:

$$\begin{aligned}
V_{By,i,j} &= V_y - x_b\left(\dot{U}_4 + \dot{\theta}_{t,y}^{\mathrm{top}}\right) - \dot{y}_{b,i,j}\sin\beta + \dot{z}_{b,i,j}\cos\beta\\
&\quad + \left(\dot{U}_2 - h_R\dot{U}_4 + \dot{z}_t^{\mathrm{top}}\right)\cos\Psi_j(t)\\
&\quad + \left(\dot{U}_3 + \dot{x}_t^{\mathrm{top}}\right)\sin\Psi_j(t)\\
V_{Bz,i,j} &= V_z - \left(\dot{U}_1 + h_R\dot{U}_5 + \dot{y}_t^{\mathrm{top}}\right) - \dot{y}_{b,i,j}\cos\beta - \dot{z}_{b,i,j}\sin\beta\\
&\quad - x_b\left(\dot{U}_5 + \dot{\theta}_{t,z}^{\mathrm{top}}\right)\cos\Psi_j(t)\\
&\quad - x_b\left(\dot{U}_6 + \dot{\theta}_{t,x}^{\mathrm{top}}\right)\sin\Psi_j(t)
\end{aligned} \tag{8}$$

with the wind speeds V_y and V_z being projections of the inflow wind speed V_0 in two orthogonal directions:

$$\begin{aligned}
V_y &= V_0\sin\chi\cos\Psi = V_0'\sin\chi'\\
V_z &= V_0\cos\chi = V_0'\cos\chi'\\
V_0' &= \sqrt{V_y^2 + V_z^2}
\end{aligned} \tag{9}$$

in which, χ represents the yaw misalignment angle as defined in Fig. 3.

Besides, lift and drag coefficients (C_l and C_d) in Eq. (4) should be determined employing look-up coefficient tables (C_l and C_d values with respect to AoAs), and a set of to-be-determined local airfoil AoAs (denoted as α) along the blade length direction. AOAs can be defined according to Fig. 3, and its mathematical expression is given by:

$$\alpha = \chi' - \left(\theta_t + \beta - \frac{\pi}{2}\right) \tag{10}$$

where θ_t is the airfoil sectional twist angle, and χ' is calculated as:

$$\chi' = \arctan\frac{V_y}{V_z} \tag{11}$$

For quasi-steady analysis, Eq. (11) becomes:

$$\chi' = \arctan\frac{V_{By,i,j}}{V_{Bz,i,j}} \tag{12}$$

The united aerodynamic loads $\mathrm{d}L$ and $\mathrm{d}D$ are defined in the local CS of $x_b - y_b - z_b$. The projected in-plane and out-of-plane aerodynamic loads are as follows:

$$\begin{aligned}
\mathrm{d}T &= \mathrm{d}L\cos\chi' + \mathrm{d}D\sin\chi'\\
\mathrm{d}S &= -\mathrm{d}L\sin\chi' + \mathrm{d}D\cos\chi'
\end{aligned} \tag{13}$$

The nonlinear aerodynamic method adopts Eqs. (4)–(13). Specifically, for blade tip section, $\theta_t = 0$ and $\beta = \pi/2$, thus, $\theta_t + \beta - \frac{\pi}{2} = 0$.

Aerodynamic static stall occurs when the local AoA exceeds the critical stall angle. As shown in Eqs. (10) and (12), the local AoA is influenced by $V_{By,i,j}$ and $V_{Bz,i,j}$ from Eq. (8). These variables depend on the platform motion and other structural velocity responses. Consequently, through the interplay described in Eqs. (8), (10), and (12),

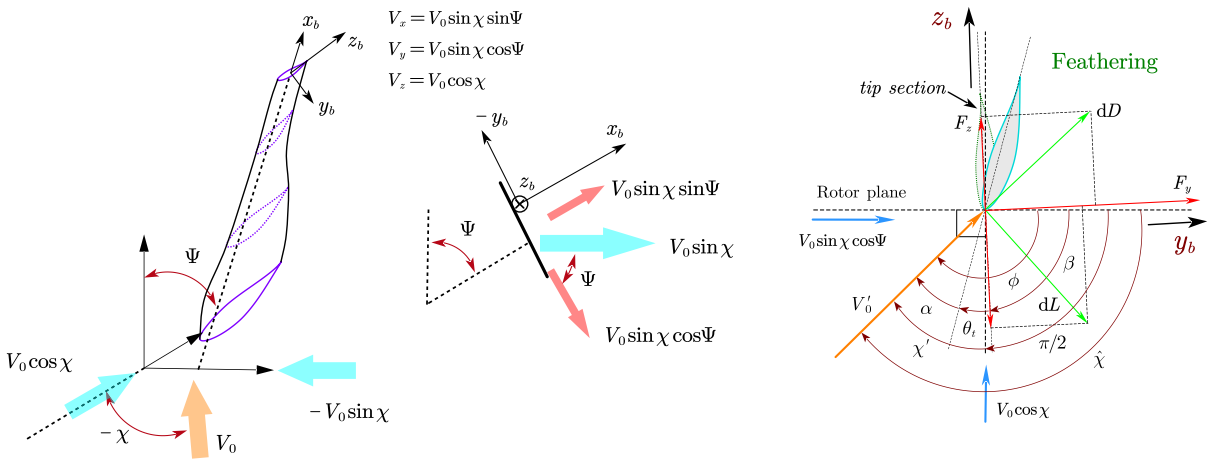

Fig. 3. Local AoA definition for a stand-still wind turbine blade airfoil.

structural dynamics (such as platform motion), and aerodynamic static stall are analytically coupled.

2.4. Hydrodynamic force and mooring line force

Previous studies have shown that the spar platform is regarded as one of the most optimal support structures for FOWT, owing to its inherent buoyancy and hydrostatic stability under both normal operating and extreme conditions, which result from its ballast-stabilized mechanism. This implies that hydrostatic stability is no longer the most controlling factor in stability analysis, but stability analysis considering hydrodynamic and aerodynamic effects should be paid more attention to. Previously developed methods for stability analysis generally ignore the hydrodynamic radiation damping despite considering the viscous hydrodynamic damping. Hydrodynamic forces include viscous damping forces and radiation history memory effects from potential flow theory; the former can be calibrated utilizing a widely used model of Morison's equation [42], while the latter can be determined using a convolutional function [38]. Besides, due to the platform's instability occurring at its natural frequencies, from the previous study of authors [30], the radiation-damping effect at low frequencies could be ignored; thus, Morison's equation is enough to account for the hydrodynamic contributions to the platform.

Moreover, mooring lines provide a rigid restoring force for the platform; this paper adopts a nonlinear mooring line simulation DLL OpenMOOR [43] as a tool to calculate the loads from mooring lines on the platform in time domain.

3. Linear model for frequency domain stability analysis

The abovementioned equation is a nonlinear dynamic system, which can capture FOWT behaviors more accurately [39]. Nevertheless, it has been proved that a linearized version of the dynamic system could be more efficient for stability analysis [9,33]. The linearized version of the dynamic system corresponding to the aforementioned nonlinear equation can be expressed as:

$$\mathbf{M}\ddot{\mathbf{x}}(t) + \mathbf{C}\dot{\mathbf{x}}(t) + \mathbf{K}\mathbf{x}(t) = \mathbf{F}^0_{\text{Aero}} + \mathbf{F}^0_{\text{Buoy}} + \mathbf{F}^0_{\text{Hydro}}(t) + \mathbf{F}^0_{\text{Moor}} + \mathbf{F}_{\text{Gra}}(t) \quad (14)$$

The updated mass matrix $\mathbf{M}$ includes hydrodynamic added mass effect from Morison's equation. Besides, the damping matrix $\mathbf{C}$ consists of the aerodynamic and hydrodynamic damping from fluid–structure interaction, as well as structural damping (including gyroscopic damping [44]). Hydrodynamic damping can arise from viscous effect and wave radiation, which has been clarified in the previous study of the authors [30]. In addition, the updated stiffness matrix $\mathbf{K}$ contains the structural stiffness and the stiffness provided by buoyancy and mooring lines. Therefore, the systematic matrices can be written as follows:

$$\begin{aligned} \mathbf{M} &= \mathbf{M}_{\text{s}} + \mathbf{M}_{\text{add}} \\ \mathbf{C} &= \mathbf{C}_{\text{s}} + \mathbf{C}_{\text{aero}} + \mathbf{C}_{\text{hydro}} \\ \mathbf{K} &= \mathbf{K}_{\text{s}} + \mathbf{K}_{\text{buoy}} + \mathbf{K}_{\text{moor}} \end{aligned} \quad (15)$$

in which the added mass $\mathbf{M}_{\text{add}}$, buoyancy stiffness $\mathbf{K}_{\text{buoy}}$ can be referred to in the previous literature [38]. Additionally, the determination of the hydrodynamic damping $\mathbf{C}_{\text{hydro}}$, and the calibration of mooring stiffness $\mathbf{K}_{\text{moor}}$ have been proposed in the previous study of the authors [30]. In this paper, the authors are devoted to determining the expression of matrices involving structural dynamics ($\mathbf{M}_{\text{s}}$, $\mathbf{C}_{\text{s}}$, $\mathbf{K}_{\text{s}}$) and the aerodynamic damping matrix $\mathbf{C}_{\text{aero}}$ for the stand-still FOWT. The expressions for $\mathbf{M}_{\text{s}}$, $\mathbf{C}_{\text{s}}$, and $\mathbf{K}_{\text{s}}$ can be found in Appendix A and the derivation for $\mathbf{C}_{\text{aero}}$ is in Section 3.1.

3.1. Linearized aerodynamic force

3.1.1. Assumption

The linearization of aerodynamic forces is based on Eq. (8). Assume that the vibrating velocities of blade elements in the y_b and z_b directions are small compared to the inflow wind velocities (V_y and V_z), the aerodynamic forces can be linearized around V_y and V_z. In other words, this assumption implies that the aerodynamic forces remain linear with respect to V_y and V_z, in the presence of perturbations $\mathrm{d}V_y$ and $\mathrm{d}V_z$. However, this assumption should be carefully examined, and it is necessary to determine the boundary at which the assumption no longer holds.

This paper treats the wind speeds V_y and V_z as independent variables, with the aerodynamic loads (such as $\mathrm{d}L$ and $\mathrm{d}D$ in Eq. (4)) as the dependent variables. To validate the assumption made, it is necessary to demonstrate that the perturbations (vibrational velocities of blade elements) in V_y and V_z is within the linear region on the aerodynamic loads.

Provided that the blade element vibrational speeds in both directions are $\mathrm{d}V_y$ and $\mathrm{d}V_z$, Eq. (8) can be rewritten as:

$$\begin{aligned} V_{By,i,j} &= V_y - \mathrm{d}V_y \\ V_{Bz,i,j} &= V_z - \mathrm{d}V_z \end{aligned} \quad (16)$$

Furthermore, by substituting Eq. (16) into Eq. (5), and subsequently inserting Eqs. (5) and (10) (with Eq. (12)) into Eq. (4), the lift $\mathrm{d}L$ can be calculated. The inclusion or exclusion of $\mathrm{d}V_y$ and $\mathrm{d}V_z$ in determining the perceived wind speed (Eq. (16)) leads to the disturbed lift, $\mathrm{d}L_{\text{dis}}$, and the undisturbed lift, $\mathrm{d}L_0$, respectively. To characterize the effect

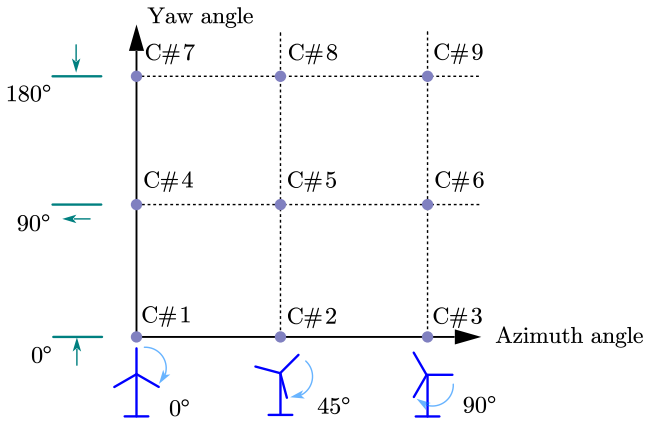

Fig. 4. Validation of small vibrating speed assumption: case definition.

of $\mathrm{d}V_y$ and $\mathrm{d}V_z$ perturbations on $\mathrm{d}L$, the difference between $\mathrm{d}L_{\mathrm{dis}}$ and $\mathrm{d}L_0$ is defined as $\delta\mathrm{d}L$, expressed as:

$$\delta\mathrm{d}L = \mathrm{d}L_{\mathrm{dis}} - \mathrm{d}L_0 \tag{17}$$

The slope of $\mathrm{d}L$, accounting for blade vibration velocities, is expressed as:

$$\begin{aligned} k_{L,y} &= \frac{\delta\mathrm{d}L}{\mathrm{d}V_y} \\ k_{L,z} &= \frac{\delta\mathrm{d}L}{\mathrm{d}V_z} \end{aligned} \tag{18}$$

As long as $k_{L,y}$ and $k_{L,z}$ remain constants, or the plot of $\delta\mathrm{d}L$ versus $\mathrm{d}V_y$ (and $\mathrm{d}V_z$) forms a straight line, the assumption holds. The same hold for $\delta\mathrm{d}D$. Assuming a wind speed $V_0 = 50\,\mathrm{m/s}$, chord length $c = 2\,\mathrm{m}$, air density $\rho_a = 1.225\,\mathrm{kg/m^3}$, yaw angle $\chi \in [0°, 90°, 180°]$, azimuth angle $\Psi \in [0°, 45°, 90°]$, pitch angle $\theta_t = 0°$, and $\beta = \frac{\pi}{2}$, nine cases (C#1 ~ C#9) can be further defined in Fig. 4.

Fig. 5 presents the results of $\delta\mathrm{d}L$ versus $\mathrm{d}V_y$ (and $\mathrm{d}V_z$), demonstrating that the aerodynamic load exhibits an almost linear relationship with the blade's vibrating speed. Notably, when the blade vibration speed is below 5 m/s, all cases except for C#6 in Fig. 4 show a perfectly linear trend. These findings confirm that the assumption is valid for subsequent derivations. However, the assumption, while suitable for linearization, becomes less accurate under extreme wind speeds or transient conditions, highlighting its limitations in predicting non-linear behaviors.

3.1.2. Derivation

Based on the assumption in Section 3.1.1, all terms except V_y and V_z in Eq. (8) have small quantities, Eq. (13) therefore can be further linearized using first-order Taylor expansion:

$$\begin{aligned} \mathrm{d}T\left(V_{By,i,j}, V_{Bz,i,j}\right) = {} & \mathrm{d}T\left(V_y, V_z\right) - \frac{\partial(\mathrm{d}T)}{\partial V_y}\left[x_b\left(\dot{U}_4 + \dot{\theta}_{t,y}^{\mathrm{top}}\right) - \dot{y}_{b,i,j}\sin\beta\right. \\ & + \dot{z}_{b,i,j}\cos\beta \\ & \left. + \left(\dot{U}_2 - h_R\dot{U}_4 + \dot{z}_t^{\mathrm{top}}\right)\cos\Psi_j(t) + \left(\dot{U}_3 + \dot{x}_t^{\mathrm{top}}\right)\sin\Psi_j(t)\right] \\ & + \frac{\partial(\mathrm{d}T)}{\partial V_z}\left[-\left(\dot{U}_1 + h_R\dot{U}_5 + \dot{y}_t^{\mathrm{top}}\right) - \dot{y}_{b,i,j}\cos\beta\right. \\ & - \dot{z}_{b,i,j}\sin\beta \\ & \left. -x_b\left(\dot{U}_5 + \dot{\theta}_{t,z}^{\mathrm{top}}\right)\cos\Psi_j(t) - x_b\left(\dot{U}_6 + \dot{\theta}_{t,x}^{\mathrm{top}}\right)\sin\Psi_j(t)\right] \end{aligned} \tag{19}$$

and,

$$\begin{aligned} \mathrm{d}S\left(V_{By,i,j}, V_{Bz,i,j}\right) = {} & \mathrm{d}S\left(V_y, V_z\right) - \frac{\partial(\mathrm{d}S)}{\partial V_y}\left[x_b\left(\dot{U}_4 + \dot{\theta}_{t,y}^{\mathrm{top}}\right)\right. \\ & - \dot{y}_{b,i,j}\sin\beta + \dot{z}_{b,i,j}\cos\beta \\ & \left. + \left(\dot{U}_2 - h_R\dot{U}_4 + \dot{z}_t^{\mathrm{top}}\right)\cos\Psi_j(t) + \left(\dot{U}_3 + \dot{x}_t^{\mathrm{top}}\right)\sin\Psi_j(t)\right] \\ & + \frac{\partial(\mathrm{d}S)}{\partial V_z}\left[-\left(\dot{U}_1 + h_R\dot{U}_5 + \dot{y}_t^{\mathrm{top}}\right) - \dot{y}_{b,i,j}\cos\beta\right. \\ & - \dot{z}_{b,i,j}\sin\beta \\ & \left. -x_b\left(\dot{U}_5 + \dot{\theta}_{t,z}^{\mathrm{top}}\right)\cos\Psi_j(t) - x_b\left(\dot{U}_6 + \dot{\theta}_{t,x}^{\mathrm{top}}\right)\sin\Psi_j(t)\right] \end{aligned} \tag{20}$$

Note that $\mathrm{d}T$ and $\mathrm{d}S$ mentioned above correspond to the in-plane and out-of-plane components respectively, whereas these loads should be reassembled in the blade root (x_b-y_b-z_b):

$$\begin{aligned} \mathrm{d}F_{x,i,j} &= 0 \\ \mathrm{d}F_{y,i,j} &= \int_L \mathrm{d}T\left(V_{By,i,j}, V_{Bz,i,j}\right)\sin\beta + \int_L \mathrm{d}S\left(V_{By,i,j}, V_{Bz,i,j}\right)\cos\beta \\ \mathrm{d}F_{z,i,j} &= -\int_L \mathrm{d}T\left(V_{By,i,j}, V_{Bz,i,j}\right)\cos\beta + \int_L \mathrm{d}S\left(V_{By,i,j}, V_{Bz,i,j}\right)\sin\beta \end{aligned} \tag{21}$$

Insert Eqs. (19) and (20) into Eq. (21). Thus, the aerodynamic loads at each airfoil section can be obtained. More generally, the derived expressions can be further denoted as vectors and matrices:

$$\mathbf{F}_{\mathrm{Aerob}}^{*} = \mathbf{F}_{\mathrm{Aerob}}^{0*} - \left[\mathbf{C}_{\mathrm{Aerobb}}^{*} \quad \mathbf{C}_{\mathrm{Aerobt}}^{*} \quad \mathbf{C}_{\mathrm{Aerobp}}^{*}\right]\begin{Bmatrix}\dot{\mathbf{v}}^{\mathrm{e}} \\ \dot{\mathbf{u}}^{\mathrm{top,e}} \\ \dot{\mathbf{U}}\end{Bmatrix} \tag{22}$$

in which $\mathbf{F}_{\mathrm{Aerob}}^{*}$ is the load vector for one blade element, and it can be summarized as the form of a static aerodynamic load vector $\mathbf{F}_{\mathrm{Aerob}}^{0*}$ minus an aerodynamic damping loads vector. $\mathbf{F}_{\mathrm{Aerob}}^{0*}$ is given by:

$$\begin{aligned} \mathbf{F}_{\mathrm{Aerob}}^{0*} = \Bigg\{ & 0, \int_L \mathrm{d}T\left(V_y, V_z\right)\sin\beta + \int_L \mathrm{d}S\left(V_y, V_z\right)\cos\beta, \\ & -\int_L \mathrm{d}T\left(V_y, V_z\right)\cos\beta + \int_L \mathrm{d}S\left(V_y, V_z\right)\sin\beta, 0, 0, 0\Bigg\}^{\mathrm{T}} \end{aligned} \tag{23}$$

and the aerodynamic damping sub-matrix of one blade section is represented by:

$$\mathbf{C}_{\mathrm{Aerobb}}^{*} = \begin{bmatrix} 0 & 0 & 0 & 0 & 0 & 0 \\ 0 & c_{y_by_b} & c_{y_bz_b} & 0 & 0 & 0 \\ 0 & c_{z_by_b} & c_{z_bz_b} & 0 & 0 & 0 \\ 0 & 0 & 0 & 0 & 0 & 0 \\ 0 & 0 & 0 & 0 & 0 & 0 \\ 0 & 0 & 0 & 0 & 0 & 0 \end{bmatrix} \tag{24}$$

An example of $c_{z_bz_b}$ is given by:

$$\begin{aligned} c_{z_bz_b} = {} & -\int_L \frac{\partial(\mathrm{d}T)}{\partial V_y}\cos^2\beta - \int_L \frac{\partial(\mathrm{d}T)}{\partial V_z}\sin\beta\cos\beta \\ & + \int_L \frac{\partial(\mathrm{d}S)}{\partial V_y}\cos\beta\sin\beta + \int_L \frac{\partial(\mathrm{d}S)}{\partial V_z}\sin^2\beta \end{aligned} \tag{25}$$

Four items in Eq. (25) ($\frac{\partial(\mathrm{d}T)}{\partial V_y}$, $\frac{\partial(\mathrm{d}T)}{\partial V_z}$, $\frac{\partial(\mathrm{d}S)}{\partial V_y}$, and $\frac{\partial(\mathrm{d}S)}{\partial V_z}$) require further derivations. Their expressions are given in Appendix A.

Additionally, the total aerodynamic loads from the rotor at the tower top node—F_x, F_y, F_z, M_x, M_y, and M_z, representing translational forces and bending moments along and around the x_t, y_t, and z_t axes—can be obtained by integrating $\mathrm{d}T\left(V_{By,i,j}, V_{Bz,i,j}\right)$ and $\mathrm{d}S\left(V_{By,i,j}, V_{Bz,i,j}\right)$ over the six directions. These loads can also be expressed in vector and matrix forms as follows:

$$\mathbf{F}_{\mathrm{Aerot}}^{*} = \mathbf{F}_{\mathrm{Aerot}}^{0*} - \left[\mathbf{C}_{\mathrm{Aerotb}}^{*} \quad \mathbf{C}_{\mathrm{Aerott}}^{*} \quad \mathbf{C}_{\mathrm{Aerotp}}^{*}\right]\begin{Bmatrix}\dot{\mathbf{v}}^{\mathrm{e}} \\ \dot{\mathbf{u}}^{\mathrm{top,e}} \\ \dot{\mathbf{U}}\end{Bmatrix} \tag{26}$$

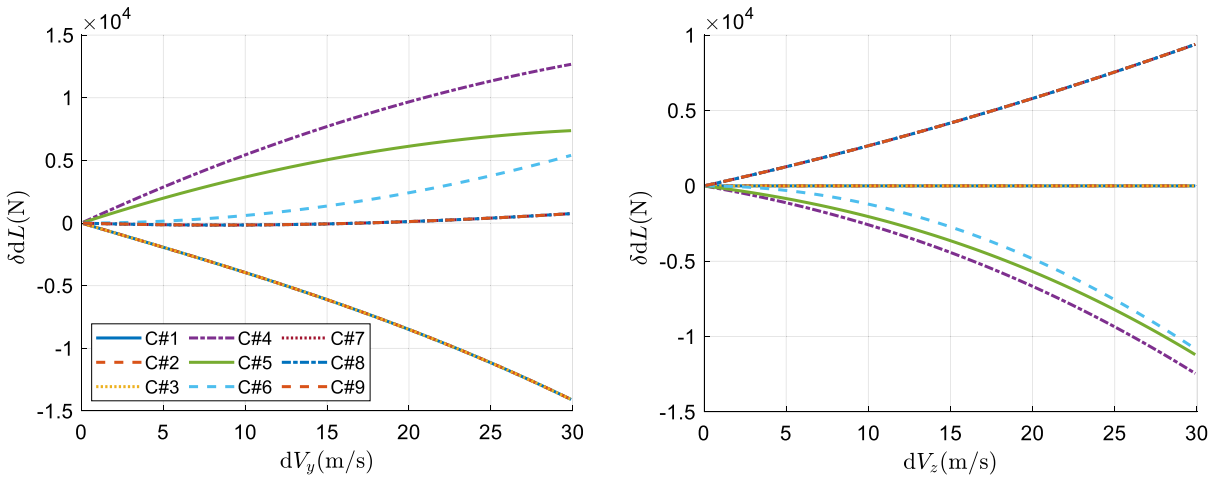

Fig. 5. Validation of small vibrating speed assumption: linear slop demonstration.

The aerodynamic loads acting on the rotor and the tower top node have been decomposed into static components and aerodynamic damping matrices. The static components are represented by $\mathbf{F}^{0*}_{\text{Aerob}}$ and $\mathbf{F}^{0*}_{\text{Aerot}}$, while the contributions from aerodynamic damping are captured using damping matrices, such as $\mathbf{C}^{*}_{\text{Aerobb}}$ and $\mathbf{C}^{*}_{\text{Aerotb}}$. The aerodynamic load $\mathbf{F}^{*}_{\text{Aerop}}$ exerted on the floating platform by the rotor is transmitted through the tower via a transformation matrix, $\mathbf{A}_{\text{pt}}$ [30]:

$$\mathbf{F}^{*}_{\text{Aerop}} = \mathbf{A}_{\text{pt}}\mathbf{F}^{*}_{\text{Aerot}} \tag{27}$$

Both the static aerodynamic force vectors and the aero-damping matrices for platform DOFs can be consquently obtained.

3.2. Linearized expressions for hydrodynamic damping and mooring line stiffness

The authors have introduced a linear and explicit way to evaluate the radiation damping based on potential flow theory and the viscous damping from Morison's equation. The detailed expressions of the viscous damping $\mathbf{C}_{\text{Morison}}$ and radiation damping $\mathbf{C}_{\text{radia}}$ can be found in Ref. [30]. Furthermore, to account for unpredicted damping contributions besides viscous damping using Morison's equation and radiation damping, the additional proportional damping $\mathbf{C}_{\text{add}}$ should also be considered in this study, and its accurate expressions can be found in Ref. [37]. Thus, the total hydrodynamic damping can be expressed as:

$$\mathbf{C}_{\text{hydro}} = \mathbf{C}_{\text{Morison}} + \mathbf{C}_{\text{radia}} + \mathbf{C}_{\text{add}} \tag{28}$$

Additionally, the stiffness of mooring lines are nonlinear and related to the platform's position. Both the previous study of the authors [30] and the NREL technical report [37] have demonstrated that the mooring line loads applied at the platform change nonlinearly when a linear moving path of the platform is given in a certain direction. To be accurate, the stiffness values of mooring lines should be taken according to the real-time position, which is a bit overcomplicated in practice. Instead, the stiffness values of the mooring lines in six directions are taken by assuming the platform is placed in its undisturbed position in the present model. The calibrated stiffness matrix is a 6×6 matrix and its elements are available in Ref. [30].

3.3. State-space method

Once the system matrices are determined, damping ratios for various modes can be conveniently calculated through complex modal analysis in state-space [40]. The original EoM are reformulated into the following state-space representation:

$$\mathbf{A}\dot{\mathbf{z}}(t) + \mathbf{B}\mathbf{z}(t) = \mathbf{0} \tag{29}$$

where

$$\mathbf{A} = \begin{bmatrix} \mathbf{C} & \mathbf{M} \\ \mathbf{M} & \mathbf{0} \end{bmatrix}, \mathbf{B} = \begin{bmatrix} \mathbf{K} & \mathbf{0} \\ \mathbf{0} & -\mathbf{M} \end{bmatrix} \tag{30}$$

The characteristic equation governs the determination of the eigenvalues and eigenvectors of the state-space model, where the eigenvectors reflect the mode shapes of the system. The characteristic equation is given as:

$$\det(\lambda\mathbf{A} + \mathbf{B}) = 0 \tag{31}$$

The complex eigenvalue λ_n corresponding to the n^{th} mode can be expressed as:

$$\lambda_n = -\zeta_n\omega_n + i\omega_n\sqrt{1-\zeta_n^2} \tag{32}$$

where ω_n denotes the natural frequency of the n^{th} mode, and ζ_n represents the damping ratio for the n^{th} mode. A negative value of $\zeta_n < 0$ indicates the presence of negative damping and signifies the instability in certain modes.

3.4. Methodological workflow

Fig. 6 presents the methodological workflow used in the study, highlighting two main approaches: the time domain approach and the frequency domain approach. Both approaches utilize a shared structural module consisting of a structural FE model and a linear hydrostatic model.

In the time domain approach, nonlinear effects from aerodynamics, hydrodynamics, and mooring dynamics are considered. These components are linearized using techniques such as Taylor expansion and Hooke's law, and the time domain responses are analyzed using the HHT-α method. Key outputs include the identification of LCOs and unstable regions.

In the frequency domain approach, the linearized models are developed to capture damping and stiffness characteristic. The state-space representation facilitates the study of dynamic properties, modal coupling, and the establishment of safety margins and control strategies.

Both approaches converge in a comparative analysis, providing a comprehensive understanding of the unstable regions and the overall system stability. Additionally, while the model effectively predicts stability characteristics, its limitations in addressing nonlinear phenomena mean that aspects such as higher harmonic generation and complex resonances are not covered in this study.

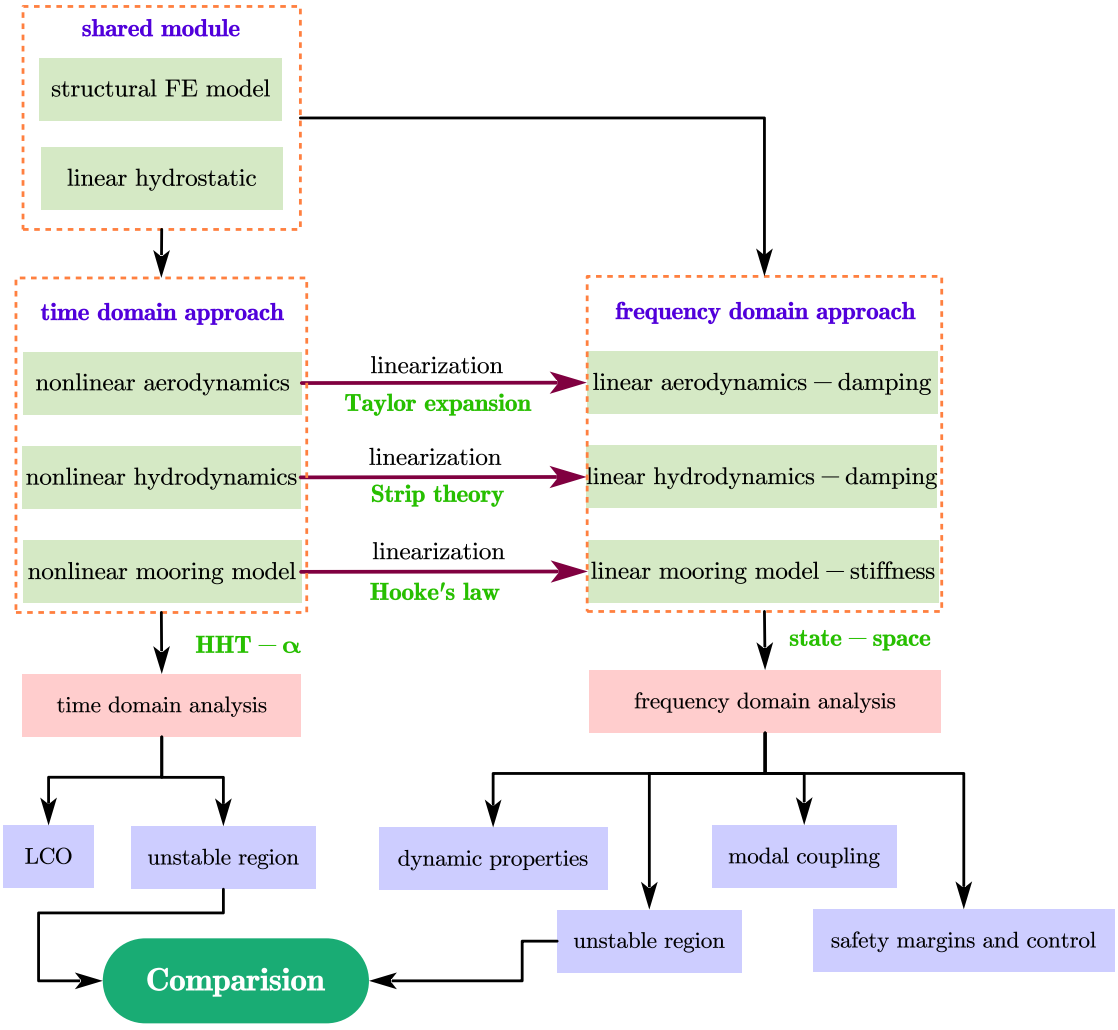

Fig. 6. Methodological workflow.

4. Model verification

Section 3 introduces an analysis tool including nonlinear and linear modules, named AeroHor-nonlinear and AeroHor-linear. This section is dedicated to presenting several verification cases to demonstrate the accuracy of the developed tool. Thus, a stand-still wind turbine at a wind speed of 50 m/s was chosen to verify this model. This paper does not consider wave loads, as the authors' previous publication [30] has already proven the efficacy of the hydrodynamic module in both frequency and time domains.

Moreover, the authors introduce an extreme condition characterized by flapwise and edgewise motion amplitudes exceeding 5 m (corresponding to velocities over 30 m/s) to validate the nonlinear aerodynamic module's capability in capturing large amplitude oscillations. In this scenario, the wind velocity is set to 50 m/s, and the yaw misalignment angle is 25°. Both cases assume the azimuth angles are zero.

4.1. Setup

A FOWT model established in OpenFAST was used to verify the new models developed in this paper. Two simplifications are made in FAST model to keep the setups in FAST consistent with the derivations: (1) the RNA center is moved to the tower top; (2) the moments of inertia of the RNA relative to the tower top are considered zero. Besides, a couple of settings are identified: (1) the mode shape coefficients are updated due to the tower top mass changes; (2) AeroDyn15 module is chosen, wake\induction model is deactivated because of the very low induction at stand-still condition; the dynamic inflow and dynamic stall are disabled for this quasi-steady study; and (3) the mooring system calculation module was chosen as "MoorDyn". To consider the influence of the control system, the pitch angles are set to 90° for the stand-still case. In the following discussion, the inflow wind speed, pitch angle, and rotor speed are kept constant for one state.

4.2. Verification

For simplicity, the verification for the linear model adopts a uniform wind velocity field, with incoming wind velocities of 50 m/s for stand-still scenarios, and the FOWT is located in still seawater. The transient responses are shown in Fig. 7. The rotor, tower top, and platform motions are benchmarked against the state-of-the-art wind turbine simulator FAST. In the time domain, satisfying agreements have been achieved, proving the accuracy of the proposed model AeroHor. Although some differences are observed in the response comparison, the overall model is accurate and sufficient for the FOWT's stability analysis.

Moreover, further analyses focus on the large amplitude oscillation on blade modes. To verify the model capability in these cases, the wind

Table 2
Natural frequencies (left: Platform and Tower modes; right: Rotor modes).

Mode	FAST (Hz)	FE (Hz)	Error (%)	Mode	FAST (Hz)	FE (Hz)	Error (%)
Surge	0.0081	0.0082	1.23	1st flap (ASY, Pitch)	0.6675	0.684	2.47
Sway	0.0081	0.0082	1.23	1st flap (SYM, Collect)	0.6993	0.709	1.39
Heave	0.0321	0.0325	1.24	1st flap (ASY, Yaw)	0.6664	0.710	6.54
Roll	0.0335	0.0339	1.19	1st edge (ASY, Pitch)	1.0793	1.071	0.77
Pitch	0.0333	0.0340	2.10	1st edge (SYM, Collect)	\	1.071	\
Yaw	0.1253	0.1223	2.39	1st edge (ASY, Yaw)	1.0898	1.087	0.26
1st FA	≈0.55 [9]	0.528	4.00	2nd flap (ASY, Pitch)	1.9223	1.980	3.00
1st SS	≈0.55 [9]	0.543	1.27	2nd flap (SYM, Collect)	2.0205	2.007	0.67

propagation direction shifts to 25° to excite large-amplitude blade instabilities. Fig. 8 shows the final comparison in blade responses between FAST and the introduced time domain module AeroHor-nonlinear in this paper. Decent agreements have been achieved in both amplitudes and phases and although some misalignments in phases are observed in flapwise, they are sufficient to conduct blade instability analyses. Obvious phase misalignment in flapwise is generated because of the error of frequency prediction. Phase disagreement can accumulate over time even with a small frequency error. Besides, structural damping ratios for blade modes are calibrated as 0.32% from 0.48% in the developed tool to pursue better agreements.

The developed model has demonstrated satisfactory performance, producing results consistent with those generated by the established FAST software. It provides an exact linear formulation, enabling detailed analysis while reducing computational demands. However, certain limitations of the proposed method should not be overlooked. For instance, while the linearization module in FAST can handle strongly nonlinear scenarios, the AeroHor-linear model cannot. Additionally, due to the low fidelity of the BEM-like theory, the model fails to capture vortex-induced vibrations, which are significantly affected by 3D flow phenomena.

As highlighted in previous studies [8], even code-to-code verifications between numerical models face significant challenges, making stability verification with experimental data and CFD-based aeroelastic models even more difficult. Therefore, this paper focuses solely on code-to-code verification. Future work will aim to incorporate comparisons with experimental data and CFD-based aeroelastic models to further validate the model presented in this study.

5. Frequency domain stability analysis

5.1. Dynamic properties

The analysis is conducted using AeroHor-linear. This section presents the natural modal properties of a 5 MW FOWT in still air and water. Mode shapes for each mode and their corresponding natural frequencies are shown in this part. The first six-order modes belong to the floating platform movements since the affiliated natural frequencies are much smaller than those of flexible tower and rotor modes. Platform rigid-body modes (not shown) are decoupled from the flexible modes of the tower and rotor because of the huge gap between the platform and flexible body frequencies. Besides, the 1st order tower FA, SS, and rotor flapwise, edgewise, and the 2nd order rotor flapwise, edgewise, and tower top FA, SS modes can be observed. Several representative tower and rotor mode shapes are shown in Figs. 9–10, respectively, and their more detailed natural frequencies can be found in Table 2, in which the FAST results are extracted from the data in Ref. [36]. These mode shape results are eigenvectors obtained with the basis of Eqs. (30) and (31), with the damping matrix $\mathbf{C}$ set to $\mathbf{0}$, and the pitch angle is 0.

The fundamental natural frequencies of the FE model, as shown in Table 2, are validated by comparing them with the results obtained from FAST, confirming their reasonability. Moreover, Figs. 9 and 10 depict an interesting phenomenon: the tower modes (including 1st and 2nd order symmetric and asymmetric modes) are deeply influenced by the rotor modes as the blade deflections in the rotor modes participate in the tower mode shapes. In contrast, the tower modes rarely affect rotor modes since the tower hardly participates in the rotor mode shapes. This is because the rotor mass mounted at the tower participates in tower vibration. Conversely, the nacelle is regarded as the boundary condition of the rotor, and the tower is placed under the nacelle. In this case, the tower is isolated because of the giant mass of the nacelle.

5.2. Quasi-steady stall-induced instability

Quasi-steady stall-induced instability is analyzed in this section by evaluating aerodynamic damping ratios for the dominant modes of a stand-still 5 MW wind turbine. It is assumed that the stand-still wind turbine may experience yaw misalignment, with the potential presence of azimuth angles. Specifically, a wind speed of 50 m/s and a yaw misalignment range of $\chi \in [-180°, 180°]$ are considered typical conditions. Meanwhile, the azimuth angle range is considered within $\Psi \in [0°, 120°]$ since this given range is overlapping with $\Psi \in [120°, 240°]$, and $\Psi \in [240°, 360°]$. The final results on aerodynamic damping ratios are given in Figs. 11, 12, and 13 for the platform, 1st order tower, and 1st order rotor modes, respectively. From which we can observe that both azimuth angle and yaw misalignment angle contribute to the aerodynamic damping since both factors have obvious impacts on the AoA of each airfoil. Damping ratios for all modes are almost symmetric concerning $\chi = 0°$ and $\Psi = 60°$ (see Fig. 14). Damping ratios keep positive at all azimuth angles once no yaw misalignment occurs. More interestingly, when we focus on sway and roll mode (Fig. 11(d)), at several yaw misalignment angles, which are $60° \sim 80°$ and $-80° \sim -60°$, the damping ratios keep negative for all azimuth angles, indicating a higher risk of instability under these circumstances. Fig. 15 presents the damping ratios for platform yaw and rotor edgewise modes at $\chi = 45°$, demonstrating that adjusting the azimuth angle can effectively help these modes avoid unstable regions. Furthermore, according to Figs. 11(a), 11(c), 11(e), 12(a), 13(a), downwind direction corresponded modes face lower risk of instability. It is also been found that platform surge, sway, roll, and pitch modes are less sensitive to the azimuth angle since their contours are more like horizontal strips. More importantly, azimuth angle $\Psi = 0°$ can be selected as the representative for further analysis since almost all modes exhibit the most prominent negative damping under this condition, indicating one of the most dangerous cases for all modes.

The fluctuation of aerodynamic coefficients should also be investigated. Fig. 16 gives a case of DU91 airfoil, it shows the mean value and perturbations of aerodynamic coefficients (patched region, acquired by calculating root mean square (RMS) values) captured by the wind tunnel experiment [45]. Within this manuscript, the values of C_l and C_d for each airfoil section adopt the mean values. Specifically, the mean values for each airfoil section are determined using the experimental data obtained from the NREL [36]. RMS values are considered the same as what is shown in Fig. 16. This assumption is acceptable because the airfoil section behaves like a bluff body at angles of attack during stall, diminishing the significance of the specific airfoil geometry's

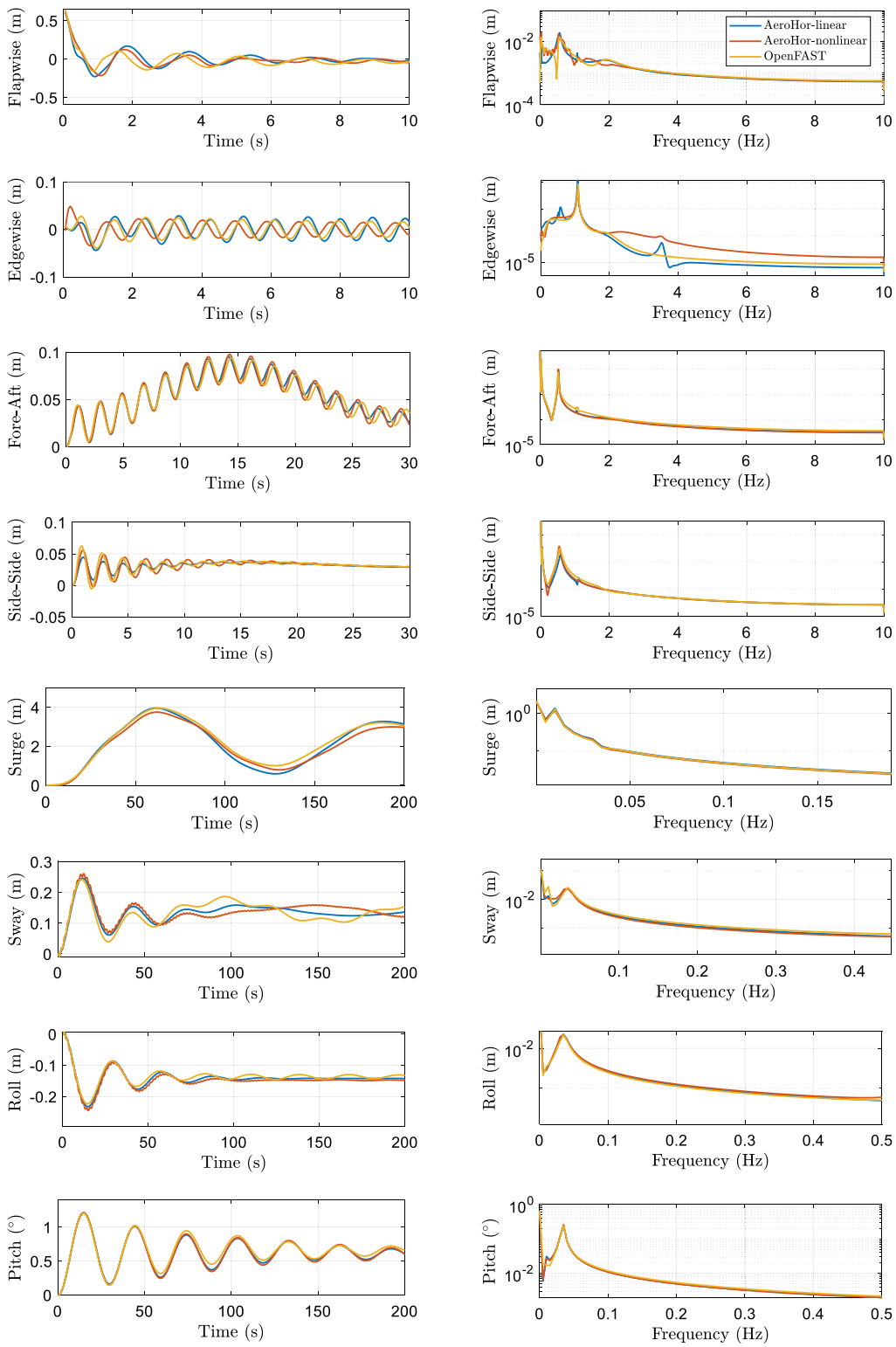

Fig. 7. Verification of the linear and nonlinear aerodynamic module against FAST. (Environment: uniformly distributed wind velocity $V_0 = 50$ m/s, pitch angle $\beta = 90°$, Azimuth $\Psi \in [0°, 120°, 240°]$, yaw misalignment angle $\chi = 0°$, still water).

impact. The determination of the mean values for C_l and C_d of the inboard circular sections can be facilitated by consulting a technical report published by NASA [46]. Finally, damping ratio value ζ_n when $\Psi = 0°$ (the first blade points upwards) considering the aerodynamic coefficients' variation are determined through the state-space method, and the results are shown in Fig. 17. It shows the aerodynamic damping ratios of major modes for FOWTs and $\zeta_n = 0$ is considered the critical condition. Aerodynamic instabilities occur while $\zeta_n < 0$ (below the dashed line in the graph), and this graph ignores the influences from structural and hydrodynamic damping. We can conclude from this picture that, if ignoring structural and hydrodynamic damping, platform sway, roll, and yaw modes, as well as tower side-side and rotor flapwise

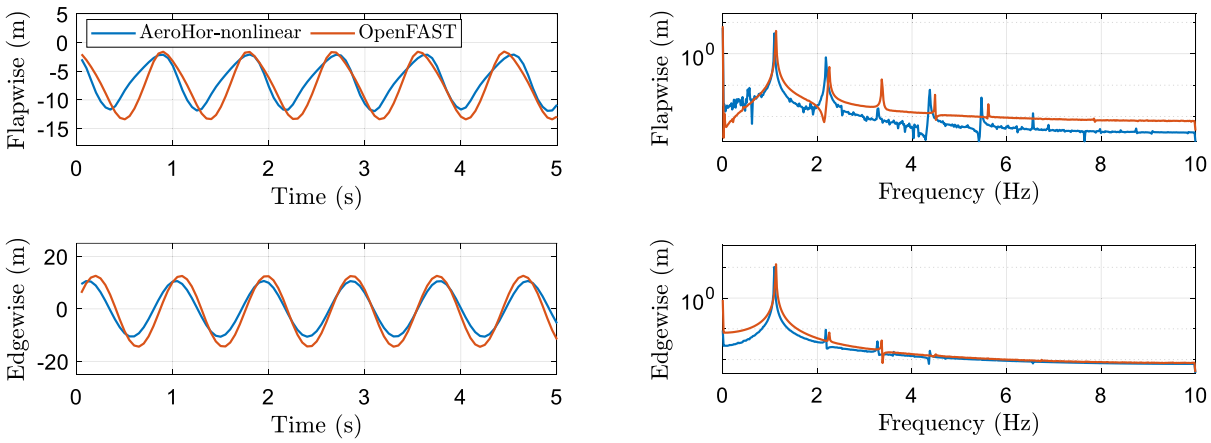

Fig. 8. Verification of the time domain nonlinear aerodynamic module against FAST under large amplitude oscillation.(Environment: uniformly distributed wind velocity V_0 = 50 m/s, pitch angle $\beta = 90°$, Azimuth $\Psi \in [0°, 120°, 240°]$, yaw misalignment angle $\chi = 25°$, still water).

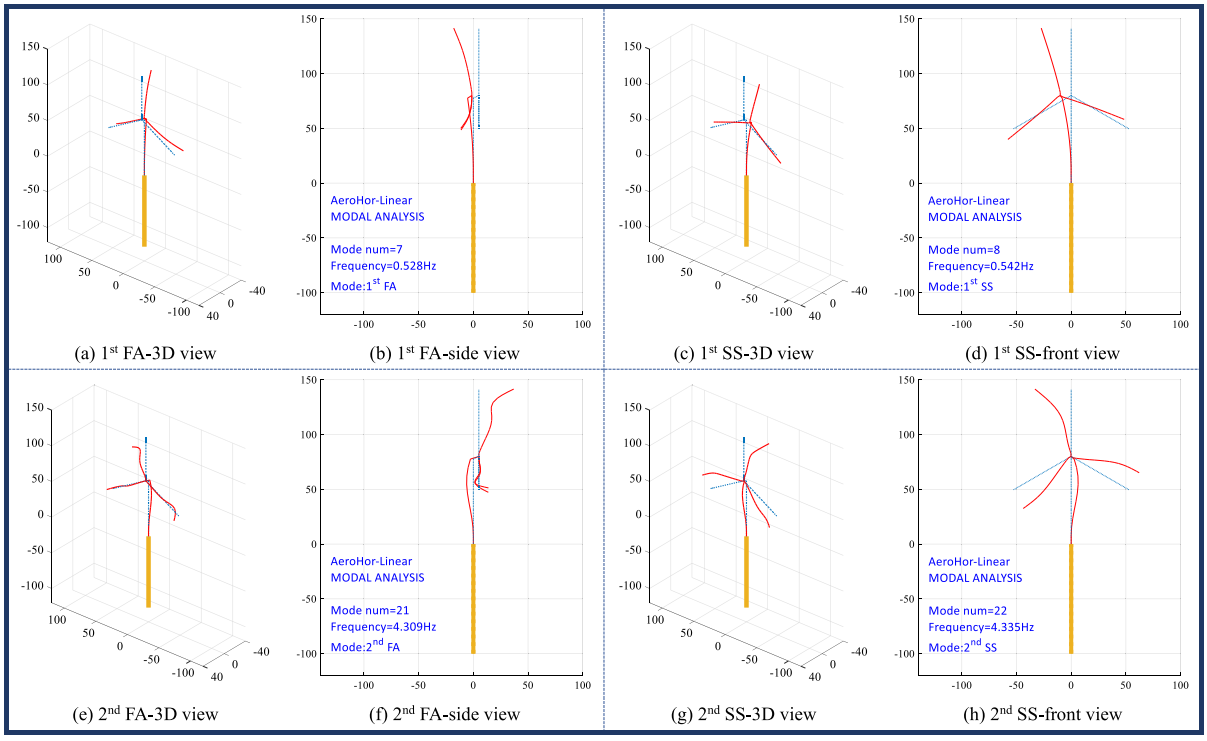

Fig. 9. Tower mode shapes (1st and 2nd order FA and SS).

and edgewise modes, face high risks of aerodynamic negative damping, and the fluctuation of aerodynamic coefficients influence the damping ratios indentified via the quasi-steady theory.

Previous analysis does not consider the influence of hydrodynamic damping. Once hydrodynamic and structural damping are included, the overall damping ratios for platform modes can significantly change. The hydrodynamic radiation and viscous damping quantification method can be referred to Ref. [30]. Assuming the FOWT is placed in such an environment with a wave height of 5 m and a wave period of 9.6 s, their hydrodynamic damping ratios are listed in Table 3. Please be aware that radiation damping is frequency-dependent, and the damping ratios listed here correspond to the natural frequencies of given modes since instabilities occur on specific modes. According to Fig. 17 and Table 3, one can notice that the overall damping ratios for the sway and roll modes are significantly greater than zero due to their exceptionally high hydrodynamic damping ratios, which represent instability that cannot possibly occur. Yaw instability should be more attention to as the minimum aerodynamic negative damping (around −2.7%) and its corresponding positive hydrodynamic damping (4.34%) reach the delicate balance. However, due to the inevitable errors in aerodynamic linearization and the rough value of the given empirical additional hydrodynamic damping, the yaw mode should also be regarded as unstable in practice.

For the tower top side-side mode, although the structural positive damping of 1% is likely to overcome the aerodynamic negative damping (around -1%), the overall side-side damping still wanders around zero. Besides, instability possibly occurs for flapwise motion but only within a limited misalignment range, which agrees with the findings of prior investigations [24,47].

The negative damping sources are explored at the blade element level to investigate the nature of the instabilities observed in the FOWT. Taking the edgewise vibration as an example, it has been proved that the diagonal element $c_{z_b z_b}$ in the damping matrix (Eq. (24)) corresponds

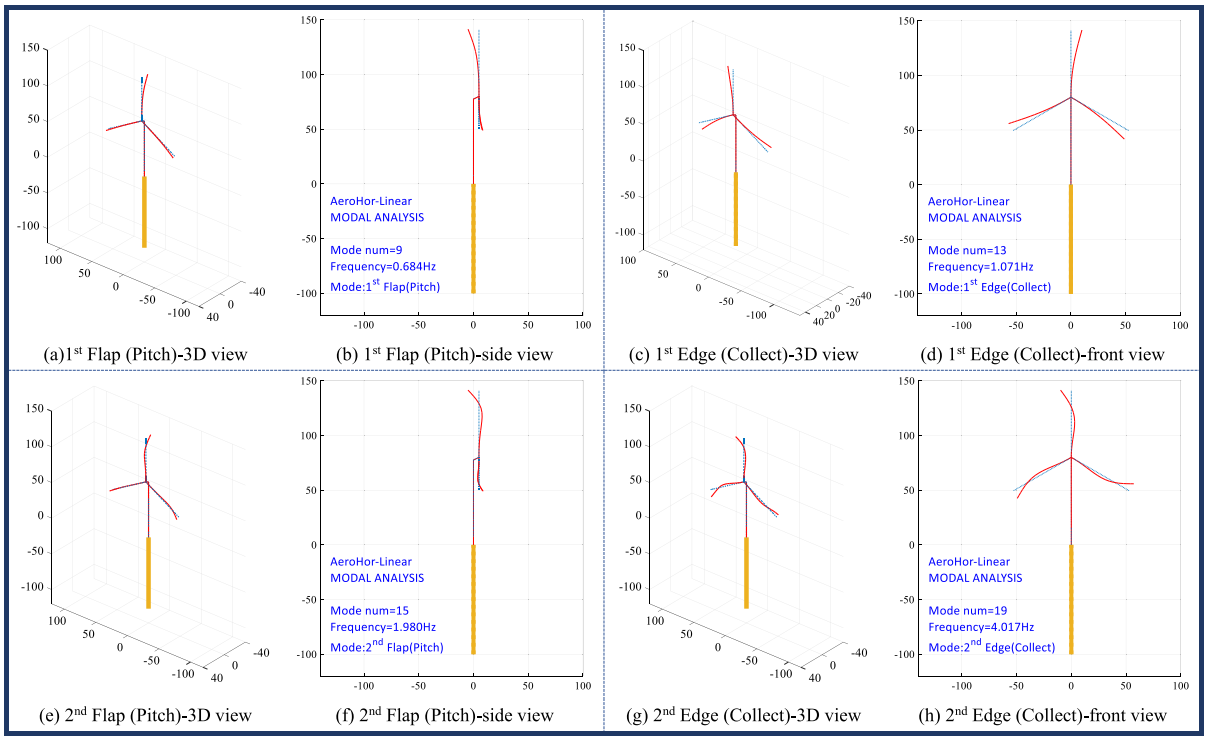

(a)1st Flap (Pitch)-3D view (b) 1st Flap (Pitch)-side view (c) 1st Edge (Collect)-3D view (d) 1st Edge (Collect)-front view

(e) 2nd Flap (Pitch)-3D view (f) 2nd Flap (Pitch)-side view (g) 2nd Edge (Collect)-3D view (h) 2nd Edge (Collect)-front view

Fig. 10. Rotor mode shapes (1st and 2nd order Flapwise and Edgewise).

Table 3
Hydrodynamic damping ratios (wave height = 5 m, wave period = 9.6 s).

Damping ratio values (%)	Surge	Sway	Heave	Roll	Pitch	Yaw
Radiation	<0.01	<0.01	≈0	<0.01	<0.01	\
Morison's viscous	16.21	17.54	\	5.25	5.26	\
Additional	6.13	6.13	7.67	\	\	4.34
Overall	22.34	23.67	7.67	5.25	5.26	4.34

to the edgewise mode, and the previous studies [12,32] have demonstrated that off-diagonal elements can be ignored. Thus, the damping ratio of the edgewise is dominated by the element $c_{z_b z_b}$. There are 17 elements for each blade, and each element corresponds to a value of $c_{z_b z_b}$. Assuming the pitch angles are 90°, we have $c_{z_b z_b} = \int_L \frac{\partial(\mathrm{d}S)}{\partial V_z}$. Thus, the values of $\int_L \frac{\partial(\mathrm{d}S)}{\partial V_z}$ can be shown in Fig. 18(a), of which the radius direction represents the blade length direction, and the rotational direction reflects the yaw misalignment angles. Interestingly, the minimum value of Fig. 18(a) can be observed from inboard sections at yaw angles around 30° and −18°. According to the expression of $c_{z_b z_b} = \int_L \frac{\partial(\mathrm{d}S)}{\partial V_z}$ in Eq. (25), the value of which are mainly controlled by $\frac{\mathrm{d}C_l}{\mathrm{d}\alpha}$, thus the minimum values of $c_{z_b z_b}$ indicate the minimum values of $\frac{\mathrm{d}C_l}{\mathrm{d}\alpha}$, reflecting the negative slope of C_l and thus, the higher occurrence possibility of stall. From experience, thick sections of the blade on the bottom are much more likely to stall, which is well in line with what Fig. 18(a) shows. Note that the actual local AoA of a specific airfoil should be the value of the yaw misalignment angle subtracted from its twist angle.

Furthermore, the modal damping $\int_L \frac{\partial(\mathrm{d}S)}{\partial V_z}\phi^2(x)$ for edgewise mode is shown in Fig. 18(b) as well, in which $\phi(x)$ represents the modal shape of the edgewise mode. Modal damping can be adopted to reflect the contribution of each element to the damping of the selected mode [40]. For example, Fig. 18(b) indicates that although the inboard sections possibly experience stall and produce negative damping for these positions, their contribution to the overall modal damping can be extremely limited since the value of $\phi(x)$ is relatively small.

5.3. Modal coupling analysis

In accordance with Eq. (24), it is evident that there exists an aerodynamic coupling between the in-plane and out-of-plane DOFs, potentially leading to a modal coupling between the in-plane and out-of-plane modes. To investigate and understand this phenomenon, our study introduces a comparative analysis.

The presence of aerodynamic damping can significantly influence the in-plane and out-of-plane mode shapes. To address this question, we employ the modal assurance criterion (MAC) [48] as a quantitative measure to assess the strength of aerodynamic damping coupling. MAC is expressed as:

$$\mathrm{MAC} = \frac{\left(\boldsymbol{\Phi}_1^{\mathrm{T}}\boldsymbol{\Phi}_2\right)^2}{\left(\boldsymbol{\Phi}_1^{\mathrm{T}}\boldsymbol{\Phi}_1\right)\left(\boldsymbol{\Phi}_2^{\mathrm{T}}\boldsymbol{\Phi}_2\right)} \tag{33}$$

where $\boldsymbol{\Phi}_1$ and $\boldsymbol{\Phi}_2$ represent the numerical mode shape vectors. When the MAC value approaches 1, it indicates a higher degree of similarity between these two modes; conversely, as it approaches 0, it signifies greater independence between each mode. The calculated MAC values are presented in Table 4 under various conditions. It reveals that, owing to the aerodynamic damping effect, the MAC values between in-plane and out-of-plane modes can surpass 0.69. This indicates a significant coupling between these modes. This coupling can also be visually represented through mode shape diagrams, shown in Figs. 19 and 20. The coupling between these two modes suggests no instability occurs in pure in-plane or out-of-plane modes.

5.4. Safety margins and control strategy

Figs. 11, 12, and 13 illustrate the aerodynamic damping characteristics of the platform, tower, and rotor modes, respectively, highlighting

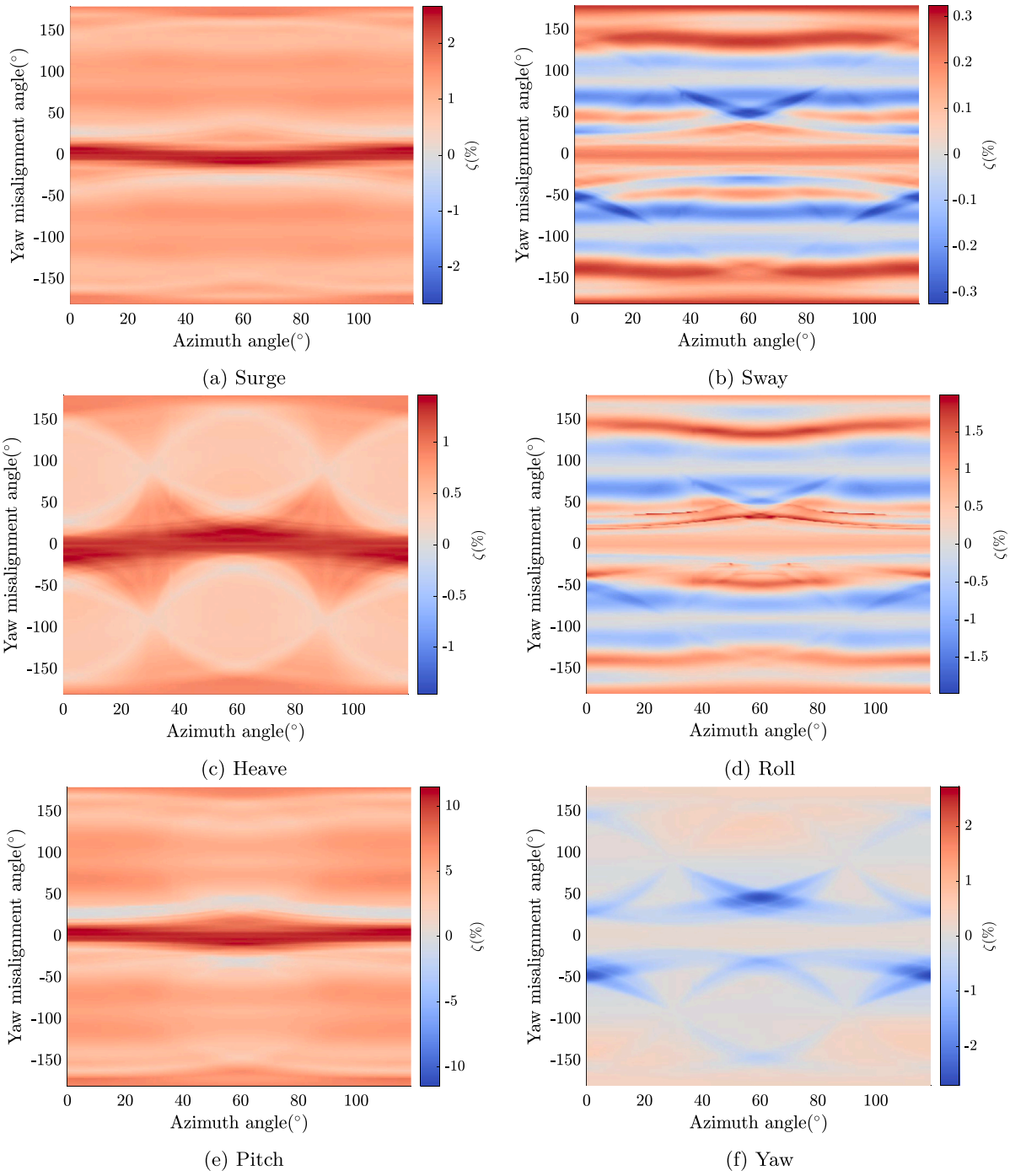

Fig. 11. Aerodynamic damping ratios for FOWT platform modes concerning azimuth angle and yaw misalignment angle (hydrodynamic damping excluded).

Table 4
MAC values.

MAC	Undamped			Aerodynamically damped		
	1st in-plane	2nd in-plane	3rd in-plane	1st in-plane	2nd in-plane	3rd in-plane
1st out-of-plane	1.25E−13	3.11E−12	0.0034	0.0017	0.0866	**0.6959**
2nd out-of-plane	1.18E−04	8.99E−04	3.01E−11	4.01E−06	**0.5949**	0.0341
3rd out-of-plane	0.0023	3.56E−05	1.99E−14	0.0795	0.0289	0.0072

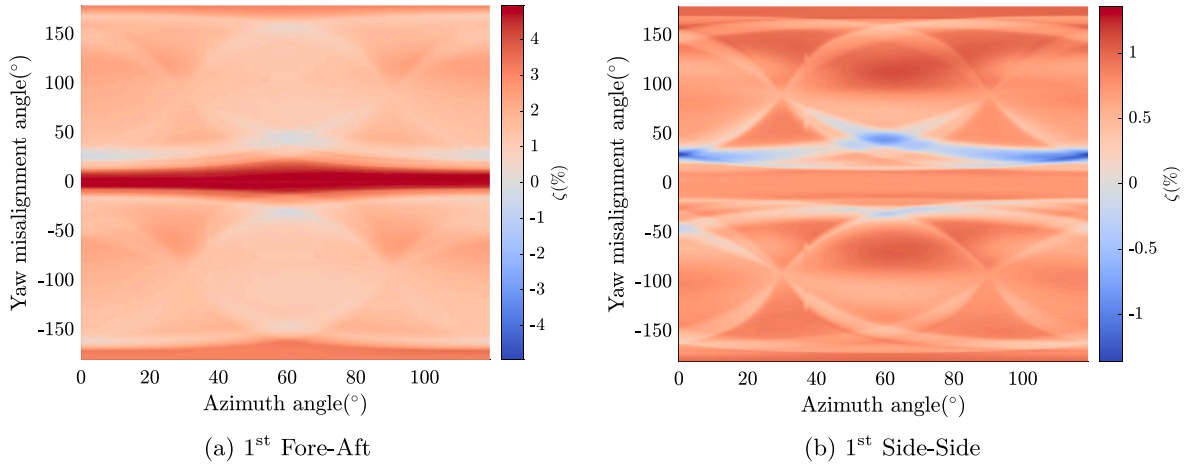

Fig. 12. Aerodynamic damping ratios for FOWT tower modes concerning azimuth angle and yaw misalignment angle (hydrodynamic damping excluded).

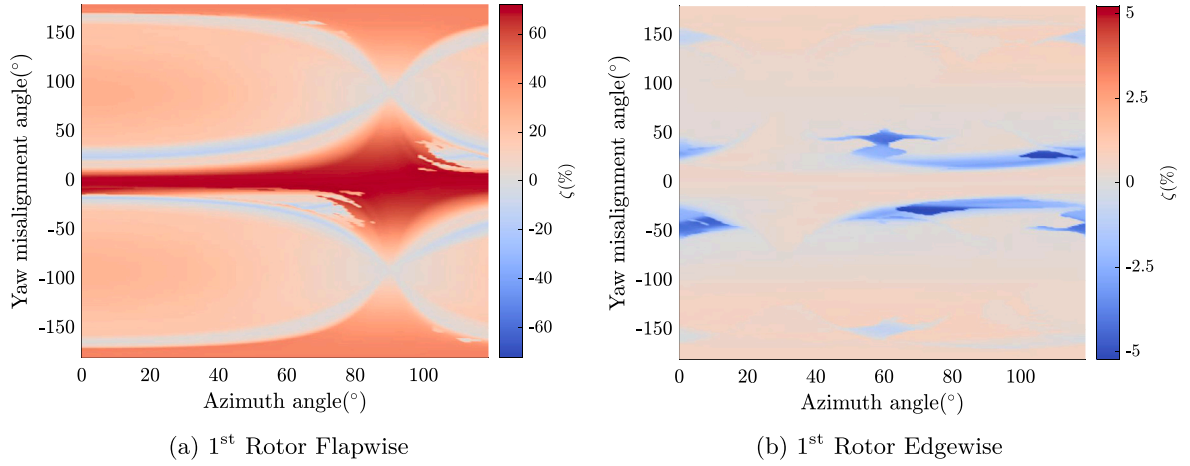

Fig. 13. Aerodynamic damping ratios for FOWT rotor modes concerning azimuth angle and yaw misalignment angle (hydrodynamic damping excluded).

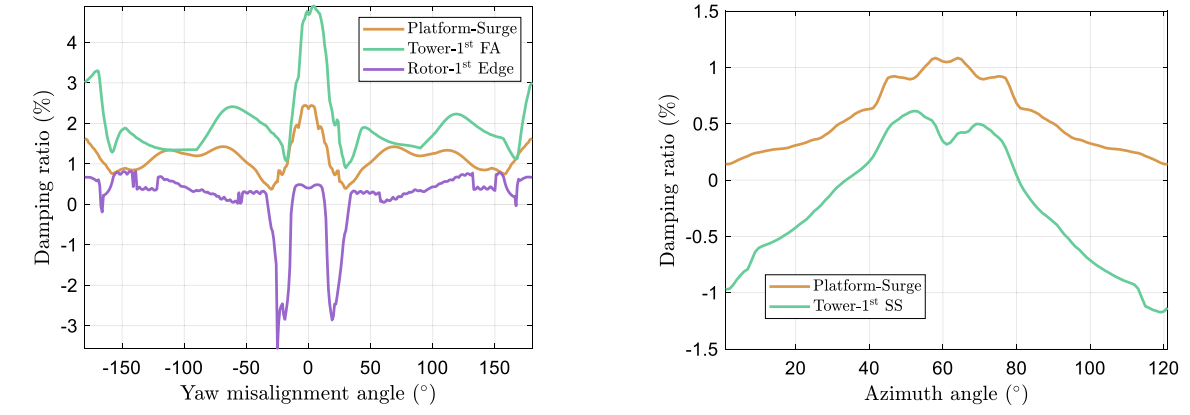

Fig. 14. Symatic features of aerodynamic damping.

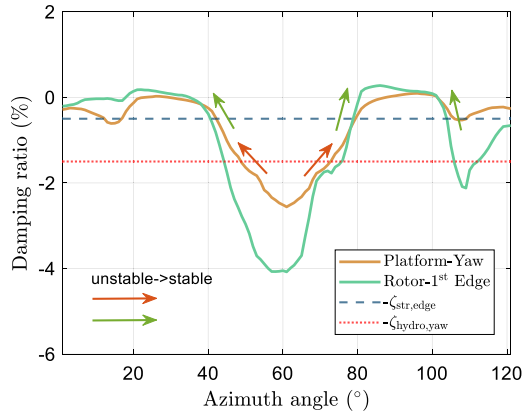

Fig. 15. Instability region and avoidance (Yaw angle $\chi = 45°$,Azimuth angle $\Psi \in [0°, 120°]$).

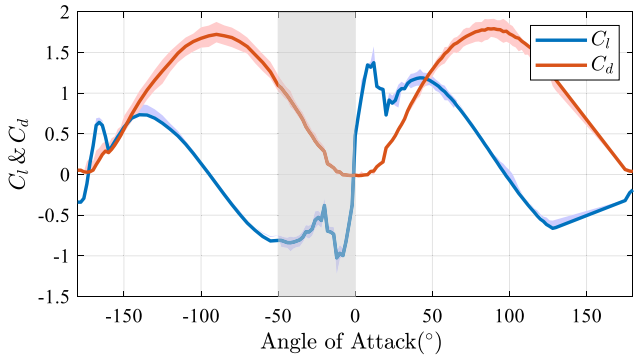

Fig. 16. C_l and C_d curves from a scaled DU91 airfoil experiment(grayed region is symmetrically determined at 0° due to experimental limitations) [45].

the regions of aerodynamic negative damping for each mode. Considering that real wind turbines operate in offshore environments, instability in any mode could result in severe damage. Therefore, it is essential to avoid the instability regions (negative damping regions, taking into account structural and hydrodynamic damping) for all modes.

As discussed earlier, the platform yaw, tower side-side, and rotor edgewise modes are particularly prone to instability. This study identifies the unstable regions for these critical modes, and the overall instability region, accounting for all modes, is presented in Fig. 21. The gray regions in the figure denote areas with a potential risk of instability in any mode. Fig. 21 illustrates the safety margins for the system. All modes remain stable within the range $\Psi \in [20°, 40°]$ at any yaw angles. Additionally, while the wind turbine is stable near $\chi = 0°$, the ranges $\chi \in [-70°, -140°]$ and $\chi \in [70°, 140°]$ exhibit broader safety bands, indicating enhanced robustness to instability. Based on these findings, the safety regions can be defined as follows:

$$\Psi_{\text{safe}} \in [20°, 40°] \quad \text{or} \quad \chi_{\text{safe}} \in \pm[70°, 140°] \tag{34}$$

Safety regions given in Eq. (34) provide an effective idea in controlling stall-induced instability: adjusting either yaw or azimuth angle can release the risk of stall-induced instability. Furthermore, due to the dynamic nature of actual environmental conditions, wind direction can change within seconds, which shows that the yaw angle control may lack robustness. Therefore, this paper strongly recommends adjusting the azimuth angle to align with the safety region. In scenarios where the azimuth angle control system is not operational, switching the yaw angle to the safety region can serve as a viable alternative. Thus, the active control strategy for stall-induced instability mitigation is given:

Algorithm 1 Active Control Strategy for Stall-induced Instability Mitigation

Input: Current/safe azimuth angle Ψ/Ψ_{safe}, yaw misalignment angle χ/χ_{safe}

procedure Aeroelastic Instability Control
  Calculate the real-time azimuth angle Ψ
  if $\Psi \in \Psi_{\text{safe}}$ **then**
    Exit the control process.
  else
    if Azimuth angle control system is operational **then**
      Adjust Ψ to the middle value within Ψ_{safe}
    else
      if $\chi \notin \chi_{\text{safe}}$ **then**
        Switch χ to the nearest middle value within χ_{safe}
      end if
    end if
  end if
end procedure

6. Aeroelastic stability evaluation in time domain

6.1. Analysis of blades

6.1.1. Limit cycle oscillations-LCOs

Figs. 11, 12, and 13 reveal the possibility of stall-induced instability utilizing the linear analysis frame. However, once the vibration occurs, due to the high frequencies of blade vibrations (around 0.67 Hz and 1.08 Hz for 1st order flapwise and edgewise, respectively), even a vibration with an amplitude of 2 m can produce a high velocity of more than 10 m/s, which means that the small blade velocities assumption is not valid. Thus, in this section, the authors adopt AeroHor-nonlinear to simulate the actual dynamic behavior of a blade, and a structural damping ratio of 0.32% is considered. In this case, the FOWT is placed in still water, the azimuth angle gives 0° and the inflow wind speed is considered 50 m/s. Aerodynamic and hydrodynamic loads are simulated through nonlinear theories in Section 3. Please also note that hydrodynamic damping effects are inherently considered without requiring special mention. Fig. 22 gives an example under the yaw misalignment angle of 25°, which corresponds to a condition with significant aerodynamic negative damping in Fig. 17, and the LCOs are found in this unstable region. LCOs happen within the rotor in-out-of-plane. Moreover, the PSD of both flapwise and edgewise DOFs are also given in Fig. 22, from which we observe that both flapwise and edgewise DOFs mainly vibrate at the first-order edgewise frequency.

Fig. 23 also demonstrates a similar phenomenon using Lissajous curves in other working conditions. Specifically, at the yaw misalignment angles of 14°, 20°, and 28°, the occurrence of LCOs can be observed. These LCOs indicate sustained oscillations in the system, suggesting the negative damping does not cause divergent vibration under these specific yaw misalignment angles. More interestingly, according to Fig. 13(b), the instability region concerning the yaw misalignment angle also depends on the azimuth angle. To be specific, instability may disappear at the yaw misalignment angle around 50° when the blade is pointing upward (azimuth angle $\Psi = 0°$) but occur at the scenario of azimuth angle $\Psi = 60°$. Time domain analyses can strengthen this conclusion: give the yaw misalignment of 50° and two azimuth angles of 0° and 60°. Their responses are shown in Fig. 24. The vibration tends to be a constant point in the plane when the azimuth angle equals 0° while the response reaches stable LCO when the azimuth angle equals 60°. The above-described phenomenon is consistent with the conclusion indicated in Fig. 13(b), which can account for the rationality of the linear theory.

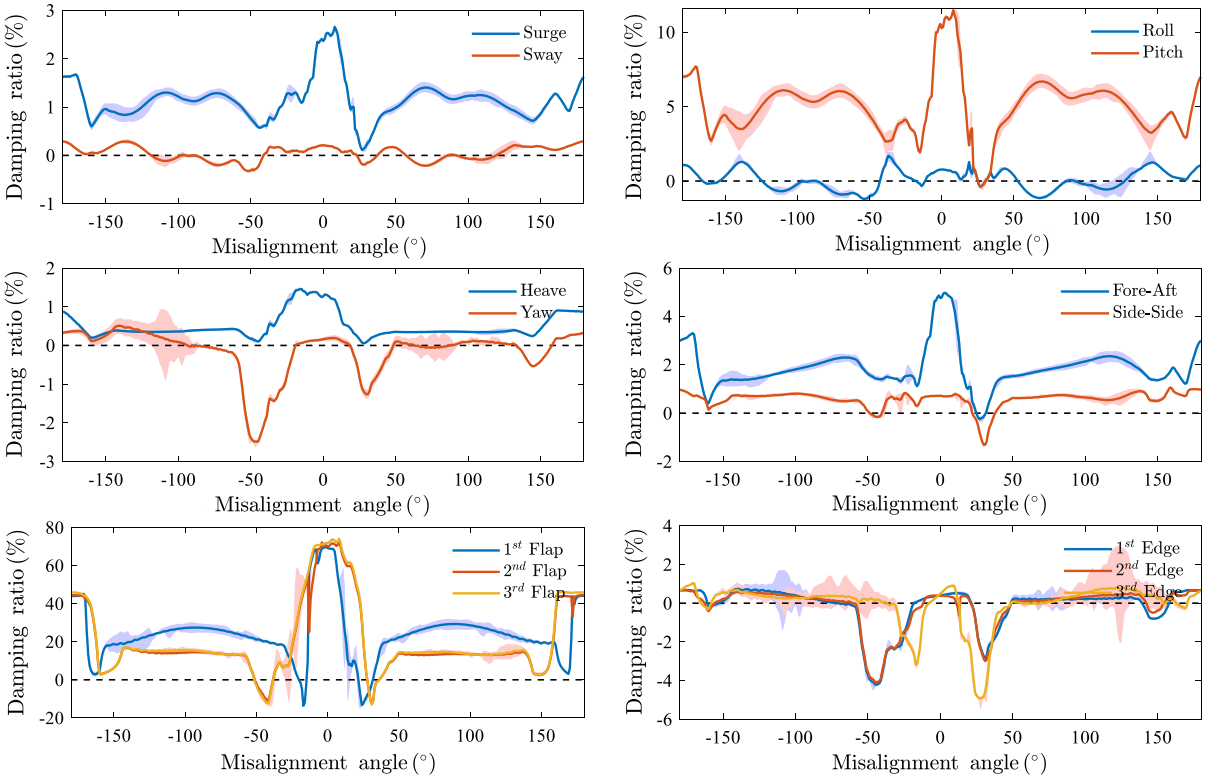

Fig. 17. Aerodynamic damping ratios for an NREL OC3 5 MW stand-still wind turbine platform modes with wind speed $V_0 = 50$ m/s, yaw misalignment angle $\chi \in [-180°, 180°]$, azimuth angle =0° (hydrodynamic damping excluded).

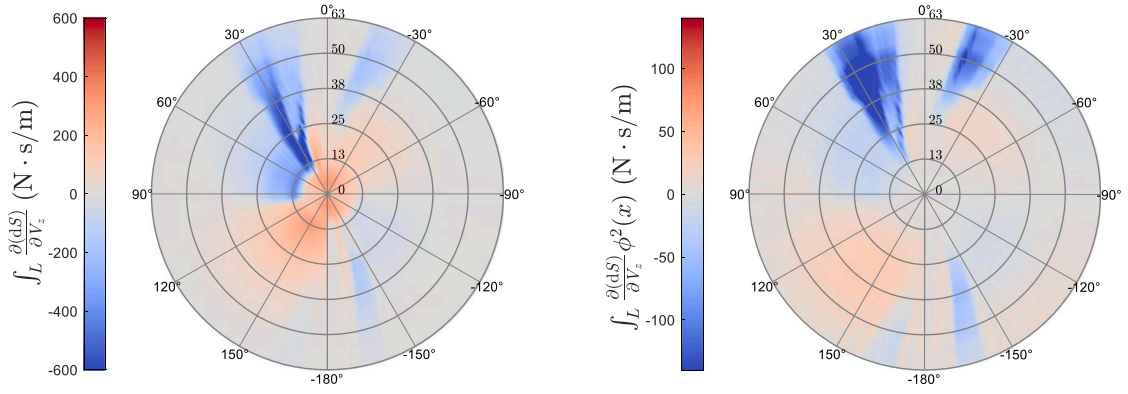

(a) edgewise aerodynamic damping coefficient (b) edgewise modal damping coefficient

Fig. 18. Damping coefficient $\int_L \frac{\partial(\mathrm{d}S)}{\partial V_z}$ and modal damping coefficient $\int_L \frac{\partial(\mathrm{d}S)}{\partial V_z}\phi^2(x)$ (wind speed $V_0 = 50$ m/s, yaw misalignment angle $\chi \in [-180°, 180°]$).

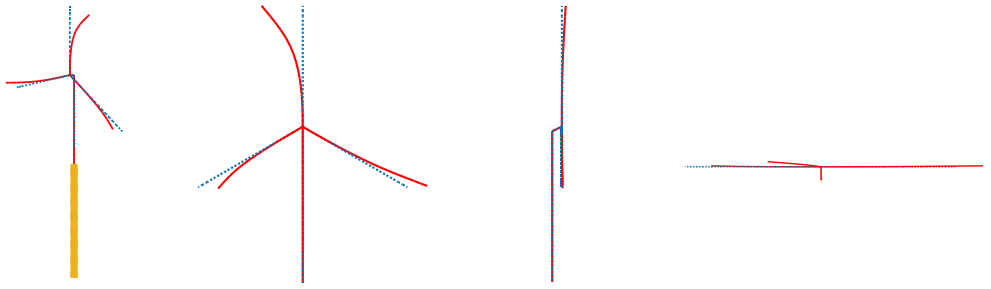

(a) 3D view (b) Front view (c) Side view (d) Top view

Fig. 19. Coupled mode of 1st order in-plane vibration (mode 9).

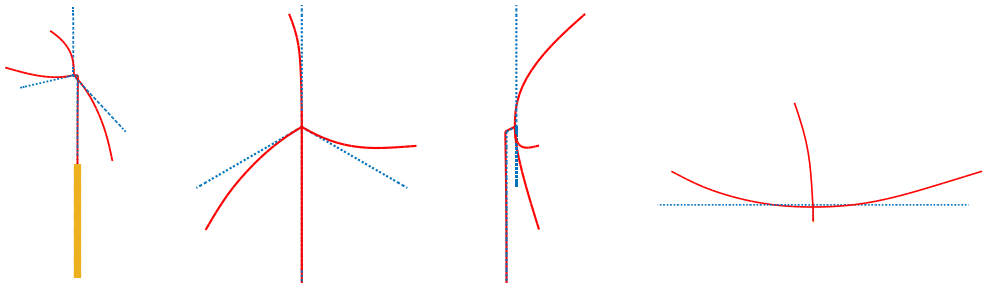

(a) 3D view (b) Front view (c) Side view (d) Top view

Fig. 20. Coupled mode of 3rd order out of plane vibration (mode 14).

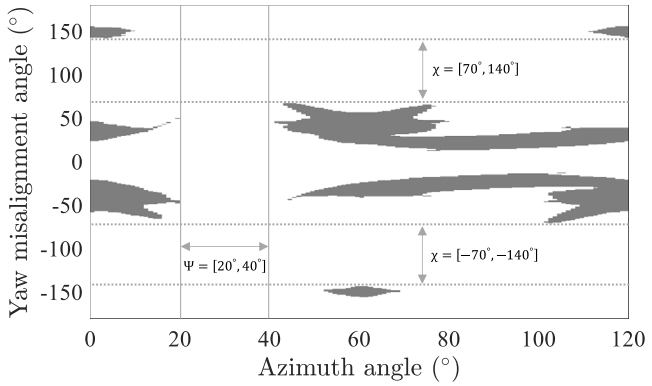

Fig. 21. Stable and unstable regions considering multi-modes (platform yaw, tower SS, and rotor edgewise), hydrodynamic damping for yaw is 1%, SS structural damping is 1%, and edgewise structural damping is 0.477%. (Note: gray region represents the unsafe region).

6.1.2. LCO contours

To gain further insights into the limit cycle motion of the blade tip at various yaw angles and wind speeds, time domain simulations of blade responses are conducted across a range of yaw angles from 0° to 50° and wind speeds from 26 m/s to 50 m/s, while the azimuth angle keeps 0°. The amplitudes of the LCOs were extracted, representing the stable vibration state with limited flapwise and edgewise movements of the blade tips. These amplitudes are presented in Fig. 25, Fig. 25 reveals the amplitudes of the edgewise and flapwise LCOs concerning both the yaw misalignment angle and wind speed. Specifically, the LCO amplitudes (both flapwise and edgewise at a wind speed of 50 m/s) gradually increase starting from approximately 13° of yaw misalignment, reaching a peak around 31°, and then stabilizing at significantly lower amplitudes beyond 35°. For comparison, Fig. 17 presents the frequency domain aerodynamic damping results, indicating aerodynamic negative damping within the yaw misalignment range of 13° to 49°. Notably, the frequency domain results predict a broader unstable range compared to the more accurate time domain responses, indicating the frequency domain approach is more conservative.

We extracted data showing the variation of LCO with yaw misalignment at a wind speed of 50 m/s, and compared it with the wind turbine's flapwise and edgewise vibration amplitudes at rated wind speed (wind speed V_0 = 11.4 m/s, and pitch angle β = 0°). The results are shown in Fig. 26, and it is obvious that under the wind turbine's blade instability state, the flapwise and edgewise vibration amplitudes are significantly higher than those of a normally operating case (dashed line), indicating a higher risk of damage and fatigue. More importantly, the vibration frequency of flapwise DOF remains consistent with edgewise DOF (not shown). This phenomenon arises for the following reason: the flapwise mode remains stable under skewed inflow conditions, the flapwise-mode vibration gradually decreases with time, and the response is finally taken over by the edgewise movement. Therefore, to enhance the stability of the rotor, it is crucial to prioritize the stability control of the edgewise motion.

Another significant trend is the crucial role wind velocity plays in developing LCO. Specifically, when the wind velocity is below approximately 40 m/s, the blade LCO exhibits a lower risk of extreme amplitude, whereas higher wind velocities correspond to larger LCO amplitudes. This observation suggests that only the largest wind velocity could be considered, as it is sufficient for stability analysis.

It is important to emphasize that the steady-state vibrations obtained from these simulations do not represent the actual physical responses of the blades. In several cases, the observed amplitudes of the limit cycle oscillations are quite large, which may indicate the potential for severe blade damage. However, the current study does not incorporate the effects of structural nonlinearity or unsteady aerodynamics, and thus these influences fall outside the scope of this work. Consequently, the simulated responses may not fully correspond to real-world behavior. Despite this limitation, the results allow for hypotheses regarding potential blade damage. For example, if the edgewise vibration amplitude of the blade were to reach 4 m, it could be interpreted as a failure condition. Nevertheless, to achieve a more comprehensive understanding of blade dynamics and failure modes, future studies should account for structural nonlinearity and unsteady aerodynamic effects. Such research would further enhance the accuracy and applicability of the analyses presented here.

6.1.3. Comparison of frequency and time domain approaches

A comparison of instability characteristics and computational complexity across different models is provided in this section, as shown in Table 5. Instability characteristics include the instability region and maximum LCO amplitude. Compared with AeroHor-nonlinear (time domain approach), the AeroHor-linear model (frequency domain approach) predicts a broader instability region, whereas OpenFAST predicts a narrower one. The AeroHor-linear model offers more conservative predictions, indicating its reliability in practical applications. While the AeroHor-linear model cannot predict the LCO amplitude due to divergence when the overall damping is negative, AeroHor-nonlinear predicts a similar LCO amplitude (20 m) to OpenFAST (17.7 m). Furthermore, the computational complexity is quantified through execution time. The execution time for instability assessment is only 1.3 s per case for the AeroHor-linear model, while the AeroHor-nonlinear time-domain solver requires over 670 s, and OpenFAST takes 49.5 s.

These findings support the notion that linear frequency domain stability analysis and time domain analysis can offer reasonable predictions of edgewise instability in this context.

6.2. Analysis of platform

6.2.1. The influence of hydrodynamic damping

Fig. 17 indicates that the platform roll mode may experience aerodynamic negative damping at a yaw misalignment angle of 30°. However,

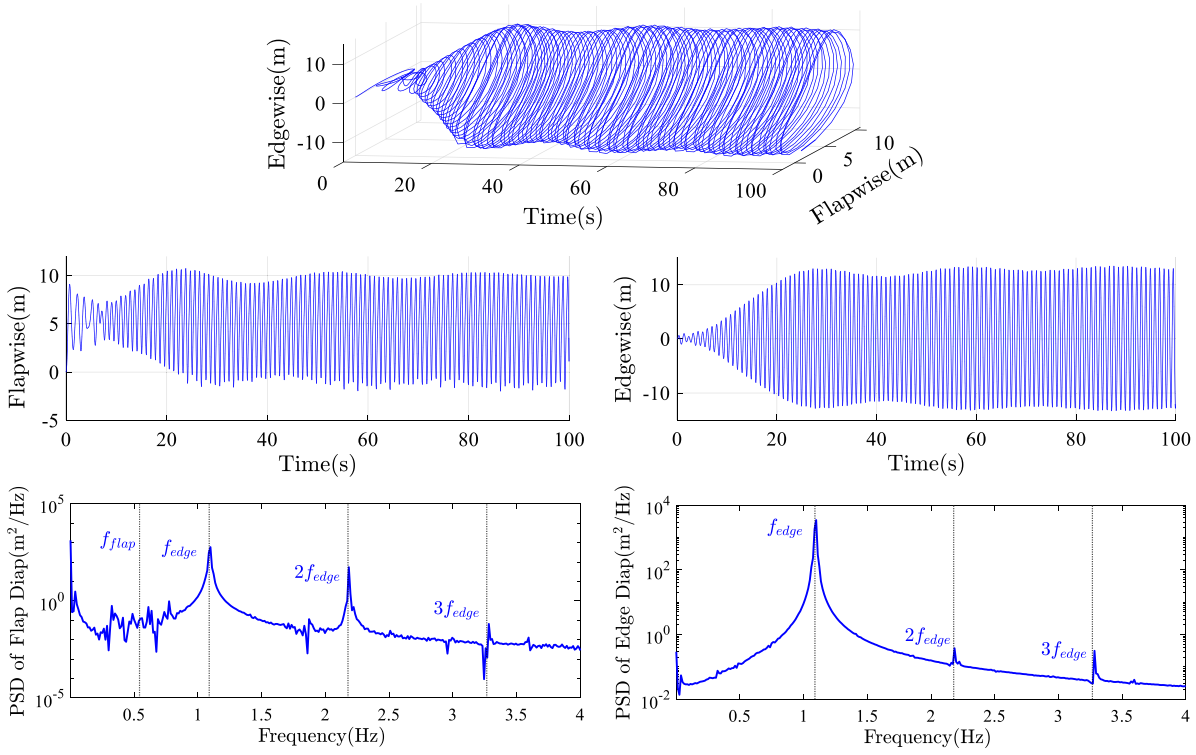

Fig. 22. LCOs and corresponding PSD of blade tip section movements, yaw misalignment angle $\chi = 25°$, inflow wind speed $V_0 = 50$ m/s, collective pitch angle $\beta = 90°$, and azimuth angle $\Psi = 0°$.

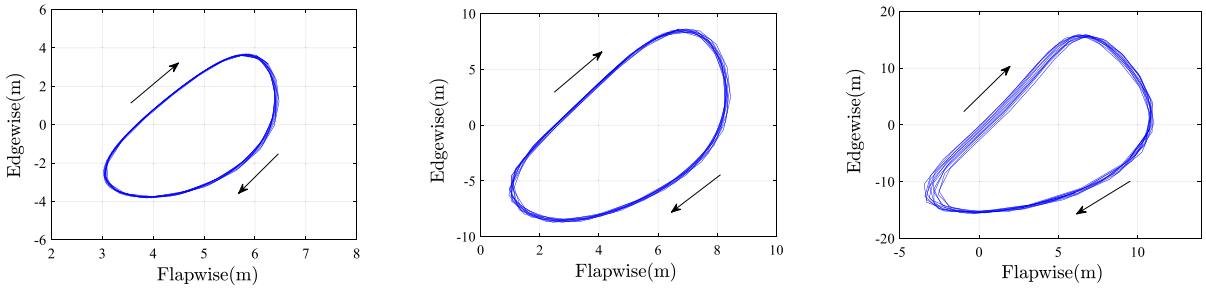

(a) Yaw angle $\chi = 14°$ (b) Yaw angle $\chi = 20°$ (c) Yaw angle $\chi = 28°$

Fig. 23. Lissajous curves: LCOs of blade tip section movement at azimuth angle $\Psi = 0°$, with yaw misalignment angle $\chi = 14°$ (a), $\chi = 20°$ (b) and $\chi = 28°$ (c), wind speed $V_0 = 50$ m/s, collective pitch angle $\beta = 90°$.

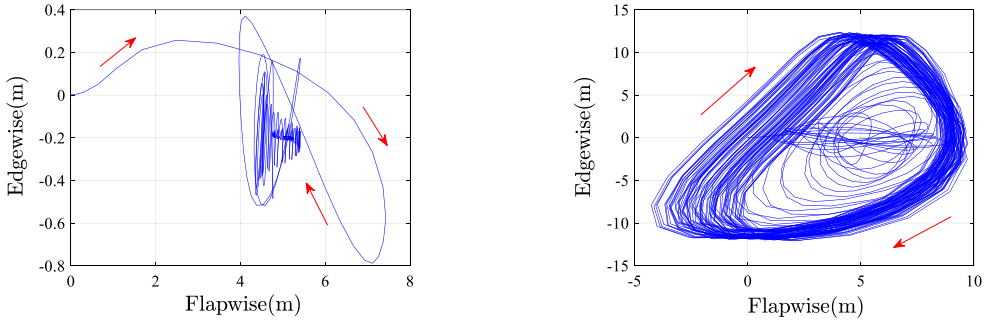

(a) Azimuth angle $\Psi = 0°$ (b) Azimuth angle $\Psi = 60°$

Fig. 24. Lissajous curves: LCOs of blade tip section movement at yaw misalignment angle $\chi = 50°$, with azimuth angle $\Psi = 0°$ (a) and $\Psi = 60°$ (b), wind speed $V_0 = 50$ m/s, collective pitch angle $\beta = 90°$.

Table 5
Comparison of instability characteristics and computational complexity across different models.

Edgewise instability	AeroHor-linear	AeroHor-nonlinear	OpenFAST
Instability region	[13°, 49°]	[13°, 35°]	[17°, 37°]
Max. LCO amplitude	Infinite	20 m	17.7 m
Execution time (for one case)	1.3 s	Simulated time: 100 s Execution time: 670.2 s	Simulated time: 100 s Execution time: 49.5 s

Notes: The AeroHor model utilizes the FE method with 372 DOFs, resulting in higher computational complexity. In contrast, OpenFAST adopts the Ritz method with only 20 active DOFs, significantly simplifying the computational process. Furthermore, AeroHor is implemented on the MATLAB platform, while OpenFAST is compiled in Fortran, contributing to the notably shorter execution time of OpenFAST.

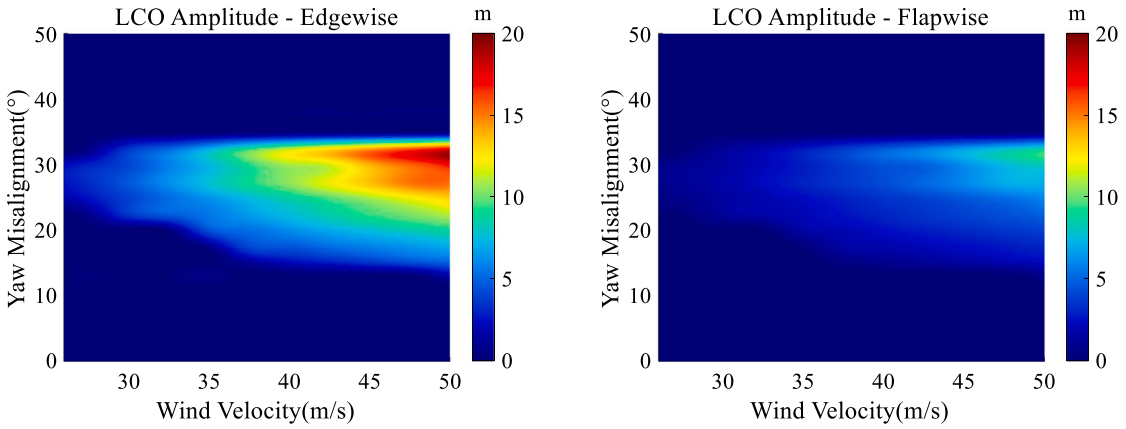

Fig. 25. LCOs amplitudes of blade tip section movements at the yaw misalignment angles $\chi = 0° \sim 50°$ with the inflow wind speed $V_0 = 26$ m/s ~ 50 m/s, collective pitch angle $\beta = 90°$, and azimuth angle $\Psi = 0°$.

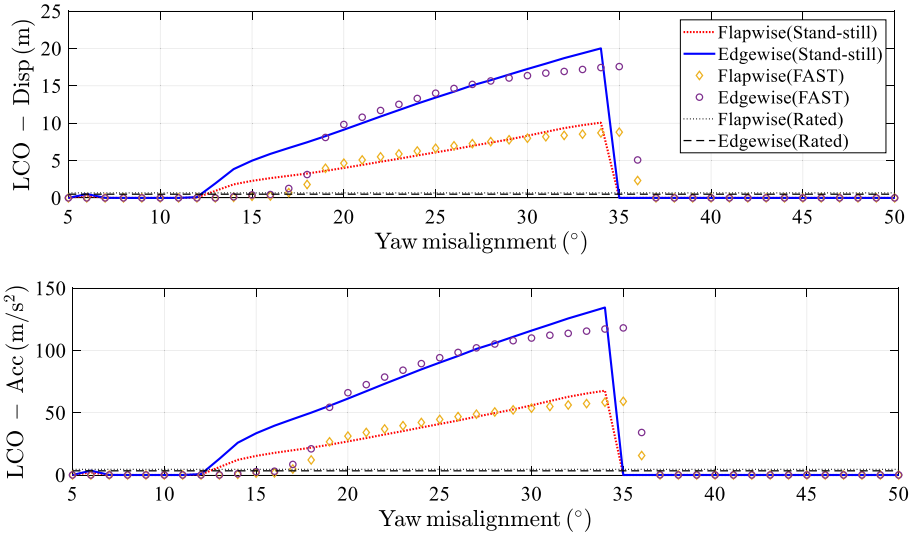

Fig. 26. LCOs amplitudes for displacement and acceleration of blade tip section at the yaw misalignment angles $\chi = 0° \sim 50°$ with the inflow wind speed of $V_0 = 50$ m/s, collective pitch angle $\beta = 90°$, and azimuth angle $\Psi = 0°$.

considering hydrodynamic damping, as detailed in Table 3 (totaling 5.25%), converts the overall damping into a positive value. To validate this assessment in the time domain, we conducted a simulation at the wind speed of 50 m/s and yaw misalignment angle of 30°. The wind turbine is placed in still water. The resulting time series response of platform roll movement, illustrated in Fig. 27, highlights the significance of hydrodynamic damping. The platform exhibits severe oscillations in the absence of hydrodynamic damping, with the maximum amplitude exceeding 15°. However, when hydrodynamic damping is considered, the vibration rapidly diminishes, affirming its crucial role in stabilizing the platform. Nevertheless, a comprehensive analysis, as previously outlined in Table 3, suggests that the positive damping contributed by hydrodynamics may not be exceptionally prominent, especially for the yaw mode. This raises the need for further investigation into the instability risk of the platform to gain a more thorough understanding of its dynamics.

6.2.2. *Blade influence on platform*

In Section 6.1, the blade modes are exposed to a higher risk of instability, characterized by significant oscillations with the potential to introduce notable perturbations in loading and vibrations for both the platform and tower. This subsection is proposed to introduce the

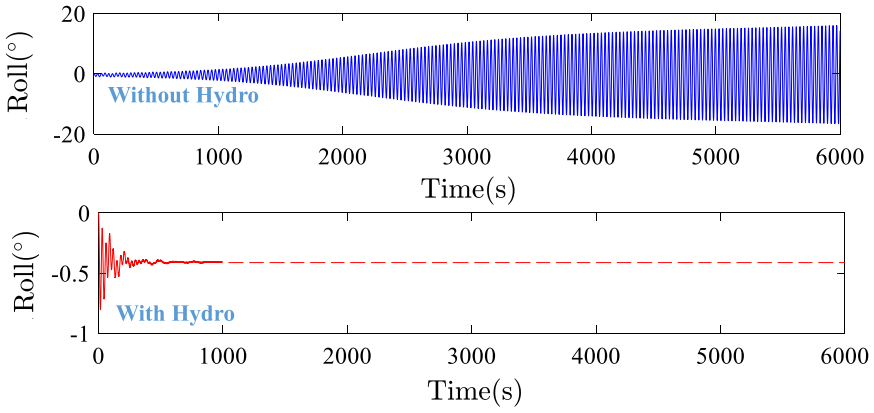

Fig. 27. Hydrodynamic effect demonstration in the time domain at yaw misalignment angle $\chi = 30°$, inflow wind speed $V_0 = 50$ m/s, blade collective pitch angle $\beta = 90°$, and azimuth angle $\Psi = 0°$.

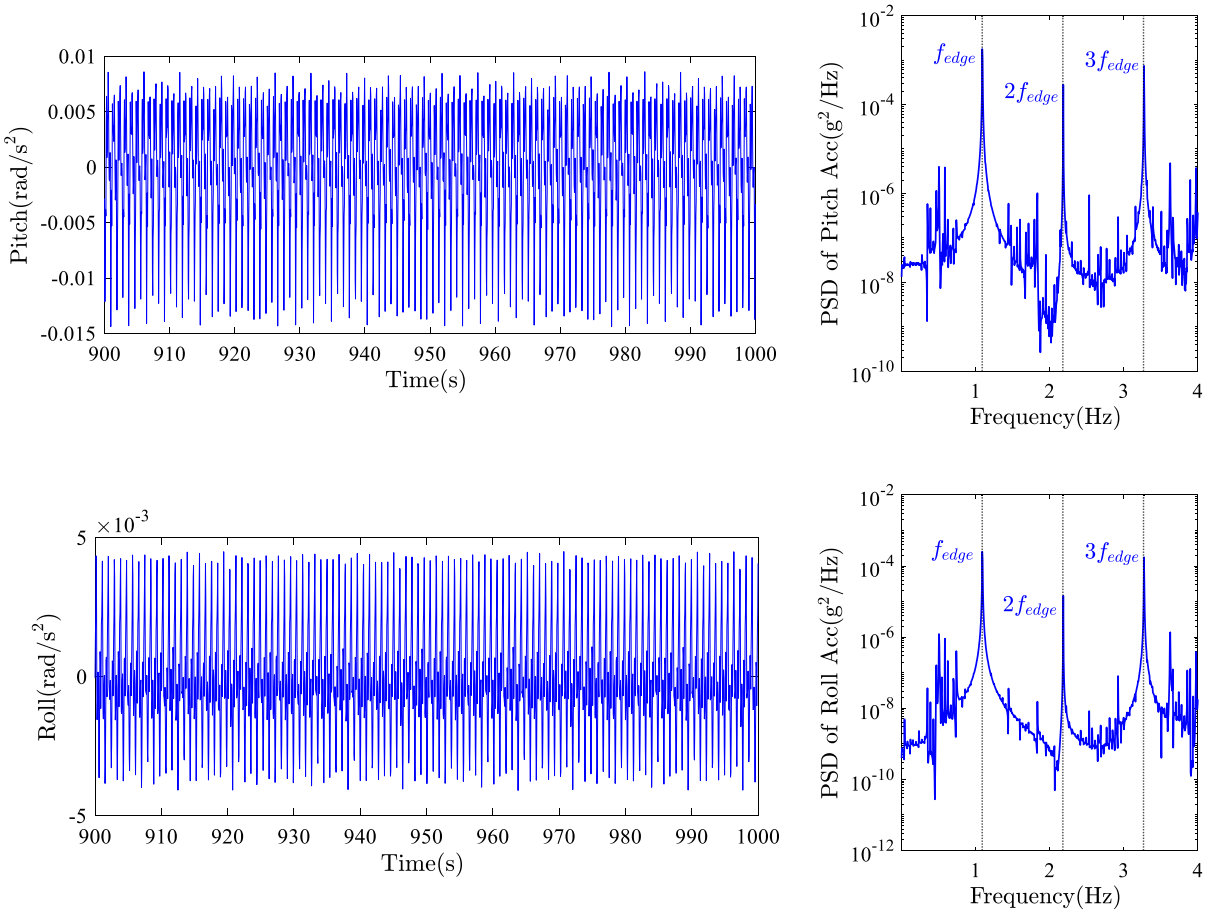

Fig. 28. Analysis of platform pitch and roll accelerations resulting from blade instability in the time domain and their corresponding PSD results: yaw misalignment angle $\chi = 30°$, inflow wind speed $V_0 = 50$ m/s, blade collective pitch angle $\beta = 90°$, and azimuth angle $\Psi = 0°$.

influence of blade instability on platform responses. The wind turbine is given the physical condition of yaw misalignment angle $\chi = 30°$, inflow wind speed $V_0 = 50$ m/s, blade collective pitch angle $\beta = 90°$, and azimuth angle $\Psi = 0°$. Meanwhile, the FOWT is placed in still sea water. As illustrated in Fig. 28, we conducted a time domain simulation to generate both platform pitch and roll accelerations when instability occurs for blades undergoing large-amplitude vibration. Besides, PSD analyses are conducted with the basis of time series data. Both time domain and frequency domain analyses reveal significant high-frequency vibrations, predominantly characterized by first-order edgewise frequencies. The frequency domain results particularly highlight the prominence of both the first-order edgewise frequency and its tripled frequency, underscoring the critical role of these two frequency components in determining the internal loads on the platform structure. However, upon scrutinizing acceleration amplitudes, the importance of high-frequency vibrations is notably reduced. This suggests that the impact of blade instability on platform vibrations may be considered negligible.

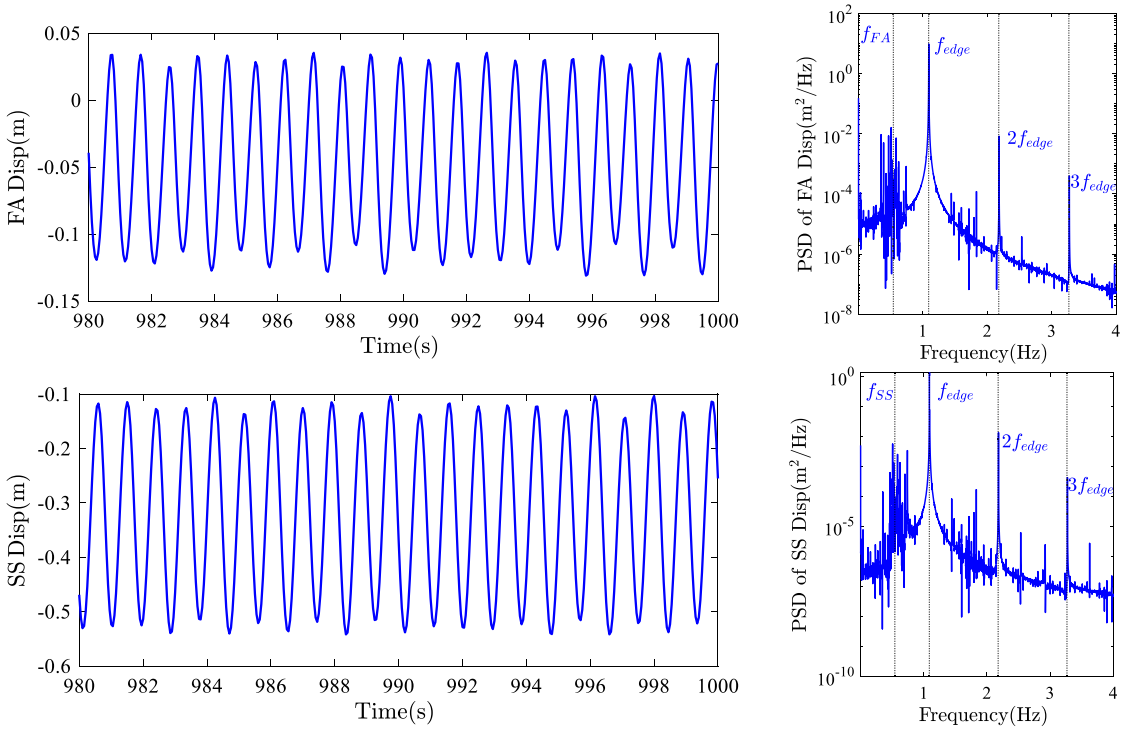

Fig. 29. Tower top FA and SS displacement responses due to blade instability: yaw misalignment angle $\chi = 30°$, inflow wind speed $V_0 = 50$ m/s, blade collective pitch angle $\beta = 90°$, and azimuth angle $\Psi = 0°$.

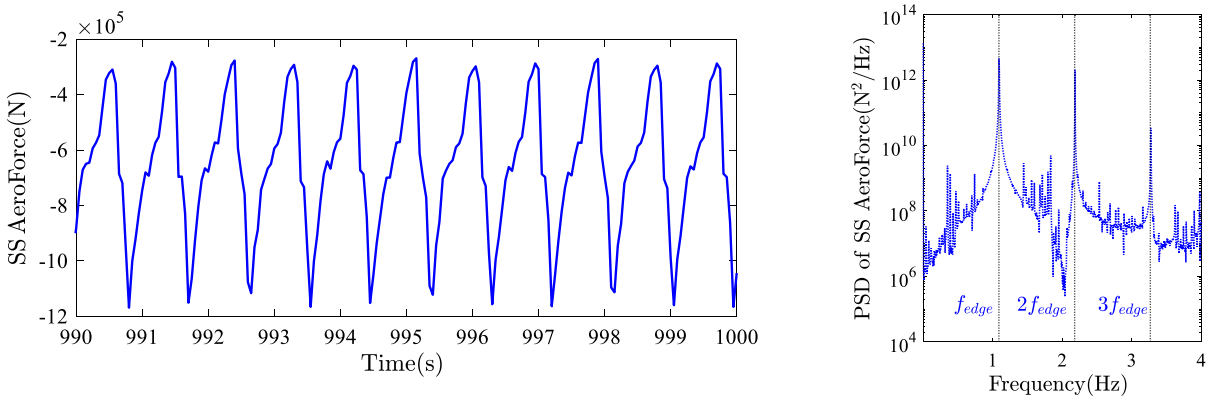

Fig. 30. Aerodynamic loading for tower top SS DOF: yaw misalignment angle $\chi = 30°$, inflow wind speed $V_0 = 50$ m/s, blade collective pitch angle $\beta = 90°$, and azimuth angle $\Psi = 0°$.

6.3. Analysis of tower

This section uses the same calculation example as the analysis in Section 6.2 but focuses on the response of tower motions with structural damping (around 1%) taken into consideration. The instability of classic towers can be attributed to insufficient damping in FA or SS modes. Still, when the vibration of the blades is very severe, it can also cause large aerodynamic forces affected by blade vibration on the tower, leading to associated tower vibration. When the blades become unstable, the vibration response of the tower is shown in Fig. 29 .

Fig. 29 depicts the time domain displacement responses at tower top, revealing it reaches a stable vibration with high frequencies. Besides, the frequency domain responses are also presented, where one can discern that the dominant frequency of the tower's SS DOF response aligns with the blade's edgewise frequency. This observation suggests that the tower's vibration is primarily a result of forced vibration induced by the significant edgewise blade vibration. Fig. 30 is presented to explain further the above finding, which illustrates the aerodynamic loads acting on the tower's top in the SS direction. As observed in the frequency domain results, the dominant frequency of the load also corresponds to edgewise frequency. This concurrence implies that the forces applied at the tower's top are predominantly driven by blade vibrations, ultimately leading to the vibration of the tower's SS mode at the edgewise frequency.

7. Conclusion

In this paper, an aeroelastic FE model with quasi-steady aerodynamic theory and hydrodynamic modules is proposed, and its linearized version is also developed. The FE model is developed using the Euler–Lagrange equation, and the linearization of the aerodynamic module is based on the first-order Taylor expansion applied to the quasi-steady formulas. The accuracy of these models has been verified against FAST. This study further conducts time domain and frequency domain stability analyses for a stand-still NREL OC3-Hywind 5 MW wind turbine using the developed nonlinear and linear models, respectively.

Linear stability analyses were conducted using the state-space method in the frequency domain. The results confirm that the stand-still FOWT faces high risks of stall-induced instabilities in blade edgewise, tower SS, and platform yaw modes. The occurrence of instability in different modes depends on both the inflow yaw misalignment and azimuth angles, and platform yaw and blade edgewise aeroelastic instabilities can be mitigated when azimuth angles are shifted to specific values. Stall-induced instabilities are mainly attributed to the aerodynamic negative damping effects on the blade outboard sections. Additionally, tower FA mode is dynamically stable due to the positive aerodynamic damping. Meanwhile, platform roll and sway modes are positively damped attributed to positive hydrodynamic damping, thus decreasing the instability risks in these modes. Furthermore, modal analysis results have unveiled the intricate coupling between the flapwise and edgewise modes, particularly highlighting the notable influence of the flapwise modes on the third-order edgewise mode. Finally, the safety margins of FOWTs are evaluated with a focus on multi-mode aeroelastic stability, and an active control strategy is proposed to mitigate stall-induced instability across all potentially unstable modes.

This study also employs the nonlinear aeroelastic model to explore the transient instability response of a FOWT in time domain. The time domain analysis shows that the blade unstable responses eventually reach steady-state LCOs when the linear stability analysis results in negative total damping of a mode. Instability regions determined through time domain approach agree well with the frequency domain approach, but the latter is more conservative. Moreover, blade instabilities induce high-frequency vibrations in the platform DOFs, with negligible amplitudes. Besides, the tower's vibration behavior is susceptible to blade instability: when blade instability occurs, it severely oscillates at its first-order natural frequency, which in turn causes the tower to experience aerodynamic forces dominated by the blade natural frequency, ultimately leading to forced tower vibrations.

The proposed methodologies help identify and mitigate stall-ind uced instability, ensuring structural safety and reliability. Both approaches can provide helpful guidance for designing robust and adaptive floating offshore wind turbines.

CRediT authorship contribution statement

Qingshen Meng: Writing – original draft, Validation, Software, Methodology, Investigation, Formal analysis. **Wei Yu:** Writing – review & editing, Supervision, Methodology, Investigation, Conceptualization. **Faming Wu:** Software, Investigation, Formal analysis. **Xugang Hua:** Writing – review & editing, Supervision, Project administration, Methodology, Investigation, Funding acquisition, Conceptualization. **Chao Chen:** Writing – review & editing, Supervision, Software, Methodology, Investigation, Formal analysis, Data curation, Conceptualization.

Declaration of competing interest

The authors declare that they have no known competing financial interests or personal relationships that could have appeared to influence the work reported in this paper.

Acknowledgments

The financial supports from the National Science Fund for Distinguished Young Scholars (No. 52025082), the National Natural Science Foundation of China (No. 52108280), the Hunan Provincial Natural Science Foundation (No. 2023JJ70001), and the Hunan Provincial Innovation Foundation for Postgraduate (No. QL20220090) are gratefully acknowledged. The financial support from CRRC Zhuzhou Electric Locomotive Research Institute Co., Ltd. (ZSFDJS-2023-00000455) is also appreciated.

Appendix A. Supplementary data

Supplementary theoretical derivations to this article can be found online at https://doi.org/10.1016/j.renene.2025.123174.

References

[1] M DeCastro, S Salvador, M Gómez-Gesteira, X Costoya, D Carvalho, FJ Sanz-Larruga, L Gimeno, Europe, China and the United States: Three different approaches to the development of offshore wind energy, Renew. Sustain. Energy Rev. 109 (2019) 55–70.

[2] J. McMorland, M. Collu, D. McMillan, J. Carroll, Operation and maintenance for floating wind turbines: A review, Renew. Sustain. Energy Rev. 163 (2022) 112499.

[3] Brian Jenkins, Arran Prothero, Maurizio Collu, James Carroll, David McMillan, Alasdair McDonald, Limiting wave conditions for the safe maintenance of floating wind turbines, in: Journal of Physics: Conference Series, Vol. 2018, IOP Publishing, 2021, 012023.

[4] Frederik Zahle, Thanasis Barlas, Kenneth Lonbaek, Pietro Bortolotti, Daniel Zalkind, Lu Wang, Casper Labuschagne, Latha Sethuraman, Garrett Barter, Definition of the IEA wind 22-Megawatt offshore reference wind turbine, Tech. Rep., National Renewable Energy Laboratory (NREL), Golden, CO (United States), 2024.

[5] Kamal Jahani, Robert G. Langlois, Fred F. Afagh, Structural dynamics of offshore wind turbines: A review, Ocean Eng. 251 (2022) 111136.

[6] Jiyuan Men, Gang Ma, Qingwei Ma, Xing Zheng, Hanbing Sun, Aeroelastic instability analysis of floating offshore and onshore wind turbines under extreme conditions, Ocean Eng. 296 (2024) 117014.

[7] Dillon M Volk, Bjarne S Kallesøe, Scott Johnson, Georg R Pirrung, Riccardo Riva, Félix Barnaud, Large wind turbine edge instability field validation, in: Journal of Physics: Conference Series, Vol. 1618, IOP Publishing, 2020, 052014.

[8] Pietro Bortolotti, Mayank Chetan, Emmanuel Branlard, Jason Jonkman, Andy Platt, Derek Slaughter, Jennifer Rinker, Wind turbine aeroelastic stability in OpenFAST, in: Journal of Physics: Conference Series, Vol. 2767, IOP Publishing, 2024, 022018.

[9] Gunjit Bir, Jason Jonkman, Aeroelastic instabilities of large offshore and onshore wind turbines, in: Journal of Physics: Conference Series, Vol. 75, IOP Publishing, 2007, 012069.

[10] A. Chizfahm, E. Azadi Yazdi, M. Eghtesad, Dynamic modeling of vortex induced vibration wind turbines, Renew. Energy 121 (2018) 632–643.

[11] Don W. Lobitz, Aeroelastic stability predictions for a MW-sized blade, Wind Energy 7 (3) (2004) 211–224.

[12] J Thirstrup Petersen, H Aagaard Madsen, A Björck, P Enevoldsen, S Øye, H Ganander, D Winkelaar, Prediction of dynamic loads and induced vibrations in stall, Tech. Rep., Risø National Laboratory, Copenhagen, Denmark, 1998.

[13] CW Acree Jr, RJ Peyran, Wayne Johnson, Rotor design for whirl flutter: an examination of options for improving tiltrotor aeroelastic stability margins, in: Annual Forum Proceedings-American Helicopter Society, 1999, pp. 997–1012.

[14] Gunjit Bir, Alan Wright, C Butterfield, Gunjit Bir, Alan Wright, C Butterfield, Stability analysis of a variable-speed wind turbine, in: 35th Aerospace Sciences Meeting and Exhibit, 1997, p. 965.

[15] Morten H. Hansen, Improved modal dynamics of wind turbines to avoid stall-induced vibrations, Wind Energy 6 (2) (2003) 179–195.

[16] M.H. Hansen, Aeroelastic stability analysis of wind turbines using an eigenvalue approach, Wind Energy 7 (2) (2004) 133–143.

[17] P.K. Chaviaropoulos, Flap/lead–lag aeroelastic stability of wind turbine blades, Wind Energy 4 (4) (2001) 183–200.

[18] Martin Hansen, Aerodynamics of wind turbines, Routledge, 2015.

[19] K Thomsen, J Thirstrup Petersen, E Nim, Stig Øye, B Petersen, A method for determination of damping for edgewise blade vibrations, Wind Energy 3 (4) (2000) 233–246.

[20] Bei Chen, Zili Zhang, Xugang Hua, Biswajit Basu, Søren RK Nielsen, Identification of aerodynamic damping in wind turbines using time-frequency analysis, Mech. Syst. Signal Process. 91 (2017) 198–214.

[21] Jason M. Jonkman, Bonnie J. Jonkman, FAST modularization framework for wind turbine simulation: full-system linearization, in: Journal of Physics: Conference Series, Vol. 753, IOP Publishing, 2016, 082010.

[22] Jason M Jonkman, Alan D Wright, Greg J Hayman, Amy N Robertson, Full-system linearization for floating offshore wind turbines in OpenFAST, in: International Conference on Offshore Mechanics and Arctic Engineering, Vol. 51975, American Society of Mechanical Engineers, 2018, V001T01A028.

[23] E Branlard, B Jonkman, GR Pirrung, K Dixon, J Jonkman, Dynamic inflow and unsteady aerodynamics models for modal and stability analyses in OpenFAST, in: Journal of Physics: Conference Series, Vol. 2265, IOP Publishing, 2022, 032044.

[24] ES Politis, PK Chaviaropoulos, VA Riziotis, SG Voutsinas, Ignacio Romero-Sanz, Stability analysis of parked wind turbine blades, in: Proceedings of the EWEC, 2009, pp. 16–19.

[25] Wrik Mallik, Daniella E. Raveh, Aerodynamic damping investigations of light dynamic stall on a pitching airfoil via modal analysis, J. Fluids Struct. 98 (2020) 103111.
[26] Fanzhong Meng, Alan W.H. Lio, Riccardo Riva, Reduced-order modelling of floating offshore wind turbine: Aero-hydro-elastic stability analysis, in: Journal of Physics: Conference Series, Vol. 2767, IOP Publishing, 2024, 062012.
[27] Jonas Lohmann, Non-linear stall-induced instability analysis of a parked rotor (Master's thesis), Delft University of Technology, Delft, The Netherlands, 2024.
[28] Feike J. Savenije, J.M. Peeringa, Aero-elastic simulation of offshore wind turbines in the frequency domain, Tech. Rep., Energy Research Center of the Netherlands, 2009.
[29] Aijun Li, Yong Liu, Huajun Li, New analytical solutions to water wave radiation by vertical truncated cylinders through multi-term Galerkin method, Meccanica 54 (2019) 429–450.
[30] Qingshen Meng, Xugang Hua, Chao Chen, Shuai Zhou, Feipeng Liu, Zhengqing Chen, Analytical study on the aerodynamic and hydrodynamic damping of the platform in an operating spar-type floating offshore wind turbine, Renew. Energy 198 (2022) 772–788.
[31] Kai Wang, Vasilis A. Riziotis, Spyros G. Voutsinas, Aeroelastic stability of idling wind turbines, Wind. Energy Sci. 2 (2) (2017) 415–437.
[32] Chuan Chen, Jingwei Zhou, Fengming Li, Endi Zhai, Stall-induced vibrations analysis and mitigation of a wind turbine rotor at idling state: Theory and experiment, Renew. Energy 187 (2022) 710–727.
[33] Morten H. Hansen, Aeroelastic instability problems for wind turbines, Wind Energy 10 (6) (2007) 551–577.
[34] Payam Aboutalebi, Aitor J Garrido, Izaskun Garrido, Dong Trong Nguyen, Zhen Gao, Hydrostatic stability and hydrodynamics of a floating wind turbine platform integrated with oscillating water columns: A design study, Renew. Energy 221 (2024) 119824.
[35] Evan Gaertner, Jennifer Rinker, Latha Sethuraman, Frederik Zahle, Benjamin Anderson, Garrett Barter, Nikhar Abbas, Fanzhong Meng, Pietro Bortolotti, Witold Skrzypinski, et al., Definition of the IEA 15-Megawatt offshore reference wind turbine, Tech. Rep., National Renewable Energy Laboratory, 2020.
[36] Jason Jonkman, Sandy Butterfield, Walter Musial, George Scott, Definition of a 5-MW reference wind turbine for offshore system development, Tech. Rep., National Renewable Energy Lab.(NREL), Golden, CO (United States), 2009.
[37] Jason Jonkman, Definition of the floating system for Phase IV of OC3, Tech. Rep., National Renewable Energy Lab.(NREL), Golden, CO (United States), 2010.
[38] Jason Mark Jonkman, Dynamics modeling and loads analysis of an offshore floating wind turbine (Ph.D. thesis), University of Colorado at Boulder, Boulder, CO (United States), 2007.
[39] Jason M. Jonkman, Dynamics of offshore floating wind turbines—model development and verification, Wind Energy 12 (5) (2009) 459–492.
[40] Roy R. Craig Jr., Andrew J. Kurdila, Fundamentals of structural dynamics, John Wiley & Sons, 2006.
[41] Barnes W. McCormick, Aerodynamics, Aeronautics, and Flight Mechanics, John Wiley & Sons, 1994.
[42] J R Morison, Joseph W Johnson, Samuel A Schaaf, The force exerted by surface waves on piles, J. Pet. Technol. 2 (05) (1950) 149–154.
[43] Lin Chen, Biswajit Basu, Søren R.K. Nielsen, A coupled finite difference mooring dynamics model for floating offshore wind turbine analysis, Ocean Eng. 162 (2018) 304–315.
[44] Pierre Blusseau, Minoo H. Patel, Gyroscopic effects on a large vertical axis wind turbine mounted on a floating structure, Renew. Energy 46 (2012) 31–42.
[45] Guanqun Xu, Wei Yu, Andrea Sciacchitano, Carlos Simao Ferreira, An experimental study of the unsteady aerodynamics of a static DU91-W2-150 airfoil at large angles of attack, Wind Energy 28 (3) (2025) e2974.
[46] Joseph J. Cincotta, G.W. Jones Jr., Robert W. Walker, Aerodynamic forces on a stationary and oscillating circular cylinder at high Reynolds numbers, Tech. Rep., 1969.
[47] Garry Garry Yuan Kwan, Investigation of idling instabilities in wind turbine simulations (Master's thesis), Delft University of Technology, Delft, The Netherlands, 2017.
[48] Randall J. Allemang, A correlation coefficient for modal vector analysis, in: Proc. of the 1st IMAC, 1982, pp. 110–116.